

Temperature-Dependent Dynamic Disproportionation in LiNiO₂

Andrey D. Poletayev^{1,2*}, Robert J. Green^{3,4}, Jack E.N. Swallow^{1,2}, Lijin An^{1,2}, Leanne Jones^{1,2}, Grant Harris³, Peter Bencok⁵, Ronny Sutarto⁶, Jonathon P. Cottom^{2,7,8}, Benjamin J. Morgan^{2,7}, Robert A. House^{1,2}, Robert S. Weatherup^{1,2*}, M. Saiful Islam^{1,2,7*}

¹ Dept. of Materials, University of Oxford, Oxford, UK

² The Faraday Institution, Harwell Science and Innovation Campus, Didcot, UK

³ Dept. of Physics and Engineering Physics, University of Saskatchewan, Saskatoon SK, Canada

⁴ Stewart Blusson Quantum Matter Institute, Univ. of British Columbia, Vancouver BC, Canada

⁵ Diamond Light Source, Harwell Science and Innovation Campus, UK

⁶ Canadian Light Source, Saskatoon SK, Canada

⁷ Dept. of Chemistry, University of Bath, Bath, UK

⁸ Present: Advanced Research Center for Nanolithography, Amsterdam, The Netherlands

* correspondence to andrey.poletayev@gmail.com, robert.weatherup@materials.ox.ac.uk, saiful.islam@materials.ox.ac.uk

Abstract

Nickelate materials offer diverse functionalities for energy and computing applications. Lithium nickel oxide (LiNiO₂) is an archetypal layered nickelate, but the electronic structure of this correlated material is not yet fully understood. Here we investigate the temperature-dependent speciation and spin dynamics of Ni ions in LiNiO₂. Our ab initio simulations predict that Ni ions disproportionate into three states, which dynamically interconvert and whose populations vary with temperature. These predictions are verified using x-ray absorption spectroscopy, x-ray magnetic circular dichroism, and resonant inelastic x-ray scattering at the Ni L_{3,2}-edge. Charge-transfer multiplet calculations consistent with disproportionation reproduce all experimental features. Together, our experimental and computational results support a model of dynamic disproportionation that explains diverse physical observations of LiNiO₂, including magnetometry, thermally activated electronic conduction, diffractometry, core-level spectroscopies, and the stability of ubiquitous antisite defects. This unified understanding of the fundamental material properties of LiNiO₂ is important for applications of nickelate materials as battery cathodes, catalysts, and superconductors.

The unexpected physics of LiNiO₂

The broad relevance of nickel-based oxides to applications such as energy storage¹, catalysis², and superconductivity^{3,4}, and the possibility to tune their properties by redox and intercalation⁵ motivates a rigorous understanding of the rich underlying physics of these materials⁶. Lithium nickel oxide, LiNiO₂, is a widely studied model layered nickelate. In catalysis, LiNiO₂ has found use as an effective

oxygen evolution catalyst⁷. In Li-ion battery cathodes, the formal Ni^{3+/4+} redox couple offers the highest conventional redox capacity for a given cutoff voltage¹. Despite this broad interest in LiNiO₂, however, to our knowledge, no single model for the electronic structure of LiNiO₂ exists that is consistent with all its observed properties.

Since LiNiO₂ has previously been comprehensively reviewed in the context of Li-

ion batteries⁸, here we provide a summary of its key behaviors, including, where relevant, comparisons to other layered alkali metal nickelates ANiO_2 and rare-earth perovskite nickelates RNiO_3 . The formally $3d^7$ low-spin ($S = 1/2$) configuration of Ni in NiO_6 octahedra is orbitally degenerate. Two possible mechanisms for relieving this orbital degeneracy (Figure 1a) are a symmetry-lowering Jahn-Teller distortion or disproportionation^{9,10}, whereby different Ni ions adopt distinct electronic and geometric local environments. Here we define disproportionation simply as the presence of distinct Ni environments and a process of interconversion between them. Considering other layered nickelates, NaNiO_2 exhibits a cooperative and collinear Jahn-Teller distortion^{11,12}, while AgNiO_2 exhibits static disproportionation to multiple distinct nickel environments¹³⁻¹⁵. RNiO_3 perovskites show similar disproportionation at temperatures below the metal-to-insulator transition, with the oxygens shared unequally between neighboring Ni ions¹⁶⁻¹⁸.

In the case of LiNiO_2 , both a dynamic non-cooperative Jahn-Teller effect^{8,19,20} and a disproportionation of Ni–O bond lengths^{21,22} have been proposed, but neither model alone accounts for all the above observations. Here we revisit the mechanism for relieving orbital degeneracy in LiNiO_2 . We focus on five characteristic behaviors influenced by the local Ni chemistry of LiNiO_2 :

1. Antisite defects, Ni_{Li} , where excess Ni occupies Li sites, are near-impossible to eliminate from LiNiO_2 , distinguishing it from other layered oxide cathodes⁸ and from the sodium analog NaNiO_2 .
2. LiNiO_2 exhibits temperature-activated p-type electronic conductivity²³. This temperature dependence indicates either Anderson localization or a small-polaron-hopping energy that decreases upon cooling. LiNiO_2 with $[\text{Ni}_{\text{Li}}] < 3\%$ appears

approximately two orders of magnitude more electrically conductive at room temperature than NaNiO_2 ²⁴, whereas all known polymorphs of AgNiO_2 are metallic^{25,26}.

3. Extended X-ray fine structure (EXAFS) measurements at the Ni K-edge are consistent with distortions of NiO_6 octahedra^{7,27,28}. These previous studies differ in the direction of the Jahn-Teller distortions assumed when modelling these spectra, and do not consider possible dynamics. Temperature-resolved neutron pair distribution function (PDF) analysis²⁹ and x-ray diffraction³⁰ show a gradual transition between cryogenic and room-temperature structures upon heating, rather than an abrupt change of phase.
4. Room-temperature Ni $L_{3,2}$ -edge x-ray absorption spectroscopy²² (XAS) and low-temperature neutron PDF data²⁹ show substantial differences between LiNiO_2 and NaNiO_2 .
5. The Ni magnetic moments in LiNiO_2 are approximately 10% too high for a spin-half $3d^7$ formal state³¹, but regain consistency with a formal $\text{Ni}^{3+/4+}$ redox process upon delithiation to 50%, i.e., for Li_xNiO_2 when $x \leq 0.5$.

Using a combination of ab initio molecular dynamics, three Ni L-edge spectroscopies, and ligand-field multiplet modelling, we show that a dynamic disproportionation model accounts for the five sets of observations above.

Dynamic Disproportionation

We first examine the behavior of Ni environments in LiNiO_2 using spin-polarized ab initio molecular dynamics simulations (Methods). At 300 K (Figure 1), the spins of Ni ions are principally distributed across three states: below $0.1 \mu_B$ ($S = 0$), near $0.86 \mu_B$ ($S = 1/2$), or near $1.57 \mu_B$ ($S = 1$). The spins rapidly convert between these three states via three

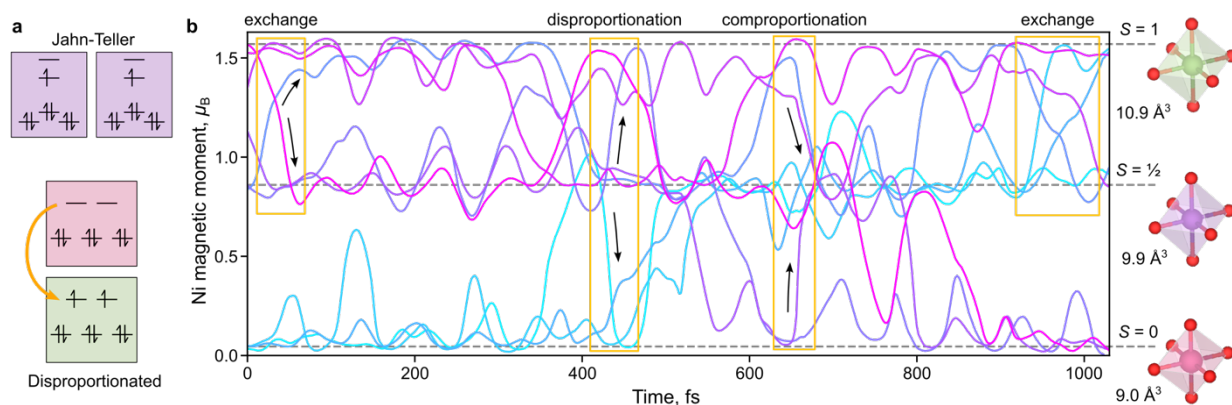


Figure 1: Ab initio simulation of spin dynamics in LiNiO₂. (a) Simplified schematic of two pathways of relieving orbital degeneracy: Jahn-Teller distortions preserving spin-half electronic structure (purple), and disproportionation (formal electron donation from pink to green). (b) Ab initio molecular dynamics trajectories of Ni spins in a layer containing nine NiO₆ octahedra over 1 ps at 300 K, colored by the initial spin (light blue to pink). Exchange, disproportionation, and comproportionation events are highlighted near 50 fs, 420 fs, and 650 fs. NiO₆ volumes are annotated for Ni states (green, purple, and pink octahedra).

processes: (i) disproportionation of $S = \frac{1}{2}$ Ni ions to $S = 1$ and $S = 0$, e.g., near 420 fs in Figure 1b, (ii) the reverse comproportionation, e.g., near 650 fs, and (iii) exchange, e.g., near 50 fs and 900 fs. All three processes preserve an average formal spin-half state of the Ni ions.

The limiting case for this three-state system is a structure consisting of three sublattices in the NiO₂ layer, each occupied by Ni exclusively in one of the three spin states²¹. In this limiting case, all NiO₆ octahedra are somewhat distorted, with the $S = \frac{1}{2}$ octahedra showing the strongest Jahn-Teller elongation, as expected. In the three-sublattice structure, all bond distances are below 2.10 Å, consistent with EXAFS^{7,27,28}. A small departure from hexagonal lattice symmetry (below 1°) is further consistent with neutron scattering and core-level spectra^{21,22,29}. We note the similarity between this limiting structure and the three transition-metal sublattices in Li(NiMnCo)O₂³², noncollinear spin models for hexagonal lattices³³, and the disproportionated structure of AgNiO₂^{13–15}.

We next evaluate the ab initio thermodynamics of spin interconversion and disproportionation in LiNiO₂. We construct free energy (F) surfaces as $F(s) = -k_B T \ln(p(s))$, where $p(s)$ is the probability distribution of coordinates, s ,

sampled over ab initio trajectories (over 10 ps, Supplementary Information), and k_B and T are Boltzmann’s constant and temperature, respectively. As coordinates, s , we use Ni magnetic moments and NiO₆ volumes, which vary by about 10% with spin states (Figure 1b). The three Ni states appear as basins in the resulting two-dimensional free energy surface (Figure 2a). The magnetic coordinate distinguishes these states more clearly than the NiO₆ volume or bond lengths (Supplementary Information), consistent with experiments on perovskite nickelates that demonstrate the primacy of the electronic coordinate³⁴.

To assess how changes in temperature affect the Ni spin populations, we performed ab initio molecular dynamics at temperatures from 100 K to 600 K. The ab initio free energy surfaces projected onto the spin coordinate (Figure 2b) show that the spin-zero and spin-one states rise in energy from 100 K to 600 K; hence, disproportionation becomes less favorable with heating. Because the local geometric and electronic coordinates are coupled, changes in the relative populations of the three states provide a possible explanation for the experimentally observed gradual evolution of lattice angle with temperature^{20,29}. At elevated temperatures, the spin-half state

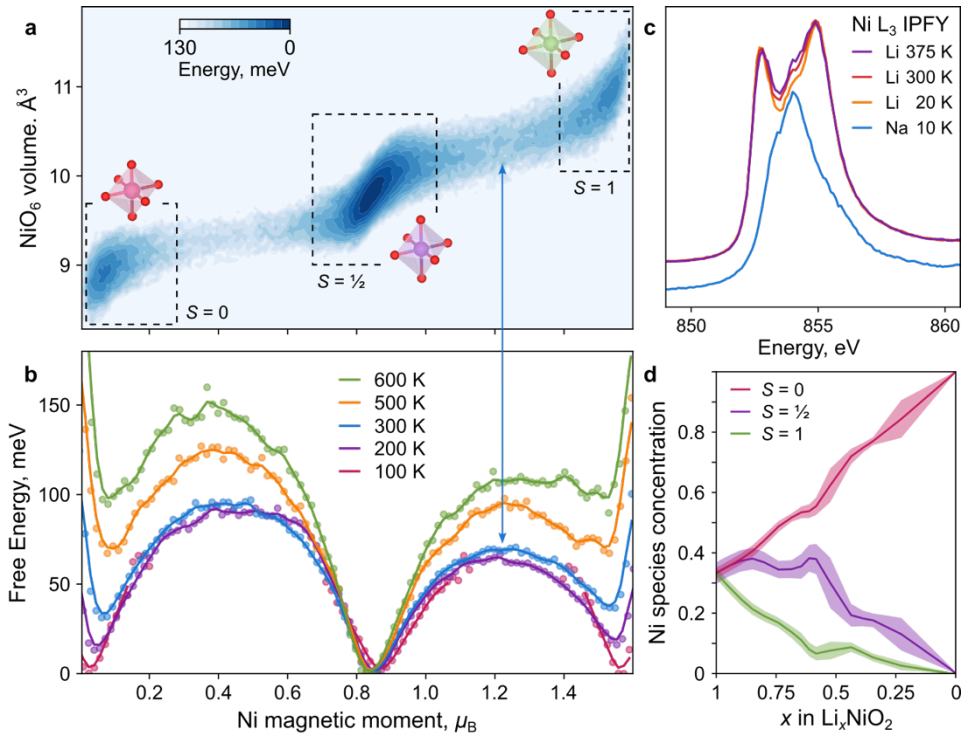


Figure 2: Temperature dependence of spin disproportionation from simulation and experiment. (a) Simulated free energy surface at 300 K, versus Ni magnetic moments and NiO₆ octahedral volume, with three basins corresponding to spin states highlighted. (b) Simulated free energy profiles versus Ni magnetic moments and temperature. The arrow connecting panels (a) and (b) highlights the saddle point between the $S = \frac{1}{2}$ and $S = 1$ states. (c) Ni L₃ edge x-ray absorption spectra of LiNiO₂ in inverse partial fluorescence yield (IPFY) mode as a function of temperature. The NaNiO₂ spectrum (blue) is offset for clarity. Fits of these spectra to three species are plotted in Extended Data Figure 1. (d) Concentrations of Ni species (green: $S = 1$, purple: $S = \frac{1}{2}$, pink: $S = 0$) during delithiation from Monte-Carlo sampling of a DFT-based cluster expansion (Methods). The shaded uncertainty values are ± 1 s.e. over eight distinct supercell sizes.

predominates, while the overall rate of transitions between states increases (Supplementary Information).

Spectroscopic Verification

We focus on the qualitative temperature trend for experimental validation. The computational prediction of an increasing fraction of $S = \frac{1}{2}$ Ni species with heating is verifiable if spin states can be distinguished experimentally. Core-level spectra are sensitive to changes in the local electronic states, and we, therefore, measured the temperature evolution of the Ni L₃-edge XAS in inverse partial fluorescence yield (IPFY) mode^{22,35} (Figure 2c). Two dominant peaks are apparent. Upon heating, these peaks decrease in intensity, while the intensity at the energies between them increases. We therefore discuss these three features in order

of increasing energy. First, the low-energy peak is characteristic of NiO-like formally 3d⁸ species ($S = 1$). Second, the interpeak energy region that grows in intensity with temperature is at an energy that matches the only peak in the corresponding spectrum of NaNiO₂ (Figure 2c, blue). Since NaNiO₂ exhibits exclusively a collective Jahn-Teller distortion of $S = \frac{1}{2}$ Ni species (Figure 1a), we ascribe this middle energy region to $S = \frac{1}{2}$ Ni species in LiNiO₂. Third, the high-energy peak could plausibly arise from a lower-spin state such as $S = 0$.

This evolution of the Ni L-edge is analogous to that observed in rare-earth perovskite nickelates RNiO₃, where double-peaked edge shapes morph into a broad and flat edge with heating across the metal-to-insulator transition^{17,18}. The overall temperature evolution of LiNiO₂ XAS spectra is weaker than predicted by the

increase in the relative proportion of $S = \frac{1}{2}$ Ni species with temperature in our ab initio simulations (Figure 2b), but the two are qualitatively consistent. We conclude that LiNiO_2 exhibits Ni-disproportionation that is both dynamic and temperature-dependent. Notably, if a Jahn-Teller distortion, collective or not, exclusively accounted for the low-temperature local geometry of LiNiO_2 , or if disproportionation were only activated with heating, then a stronger semblance to the NaNiO_2 spectra would be expected at low temperature, and the evolution of the spectra should be reversed, i.e., the low- and high-energy peaks would be expected to grow with heating.

Having experimentally validated our model of three-fold dynamic disproportionation, we use this model to predict Ni speciation upon delithiation, as occurs during battery cycling. Using grand canonical Monte-Carlo simulations (Figure 2d), we predict that during the first half of delithiation (Li content $x > 0.5$ in Li_xNiO_2), the high-spin Ni species are first to be oxidised, corresponding to net formal $\text{Ni}^{2+/4+}$ redox. For $x < 0.5$, the more expected $\text{Ni}^{3+/4+}$ redox dominates, as reported from bulk-sensitive x-ray Raman scattering³⁶. This

predicted sequence of redox events is also consistent with magnetometry³¹.

Spectral shapes of Ni species

To understand the origin of the observed changes in spectral features, we perform ligand-field charge-transfer multiplet simulations³⁷. Accounting for unequal Ni–O bond lengths arising from both the NiO_6 volume differences and the Jahn-Teller distortion predicted from simulation (Methods) affords a first-principles prediction of state-specific spectral shapes for LiNiO_2 and NaNiO_2 (Figure 3 and Extended Data Figure 1). Our predicted spectra reproduce the experimentally observed TEY and IPFY spectra for both materials. In LiNiO_2 , the $S = 1$ and $S = 0$ components account for the low- and high-energy L_3 edge peaks, respectively. This picture is consistent with both a partial disproportionation and with the usual small Ni excess in LiNiO_2 , which contributes to the $S = 1$ feature (3–5% in IPFY; Figure 3b and Extended Data Figure 1). For the spectra in Figure 2c, the proportion of $S = \frac{1}{2}$ species grows from 35% at 20 K to 41% at 375 K (Extended Data Figure 1). Even though a precise quantitative agreement may be beyond the accuracy of the predictions of density-functional theory (DFT), our experimental

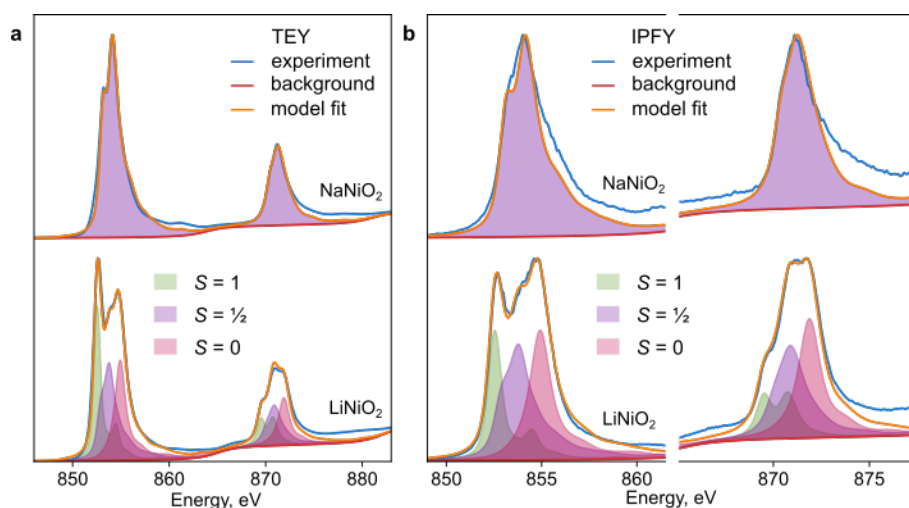


Figure 3: Decomposition of Ni L edge spectra of NaNiO_2 and LiNiO_2 . (a) TEY spectra, (b) IPFY spectra. NaNiO_2 (top) was measured at 10 K modelled exclusively using the spin-half component (Methods). LiNiO_2 (bottom) was measured at 6 K and fit to 42%-35%-23% $S = 1$, $S = \frac{1}{2}$, and $S = 0$ components, respectively, (TEY) or 33%-39%-28% of the same (IPFY). The IPFY L_2 edge was rescaled due to saturation.

results are consistent with disproportionation in LiNiO_2 and confirm the increase in the proportion of $S = \frac{1}{2}$ ions with temperature. We discuss the sensitivity of computational predictions further in the Supplementary Information.

The calculated partial densities of states for the three Ni species (Extended Data Figure 2b) verify that both $S = 1$ and $S = \frac{1}{2}$, but not $S = 0$, species contribute to the valence band edge. As with other high-valence Ni compounds³⁸, strong covalency is predicted here for the $S = \frac{1}{2}$ (mostly $d^8\bar{L}$) and $S = 0$ (mostly $d^7\bar{L}$ and $d^8\bar{L}^2$) species (Extended Data Figure 2a). A key novelty of our work is the confirmation that these formally high-valence species are present in the pristine, fully lithiated material. Therefore, we next verify the detection of $S = 1$ and $S = 0$ species with x-ray magnetic circular dichroism (XMCD) and resonant inelastic x-ray scattering (RIXS), respectively.

XMCD was performed at the Ni $L_{3,2}$ -edge under 8 T applied field (Figure 4). Circular dichroism is specifically sensitive to unpaired electrons at the Ni centers and can elucidate the competing degrees of charge transfer and covalency³⁹. The XMCD spectra thereby assist in constraining the charge transfer multiplet calculations⁴⁰. The L_3 XMCD spectra differ between LiNiO_2 and NaNiO_2 (Figure 4), mirroring the different x-ray absorption spectra, above. The LiNiO_2 L_3 XMCD spectrum has a maximum at about 1 eV lower energy and exhibits a sign change near 855 eV in IPFY. The disproportionation model reproduces the XMCD spectra of both compounds in TEY and IPFY modes. The broader dichroism features of NaNiO_2 versus the $S = \frac{1}{2}$ Ni species in LiNiO_2 are consistent with NaNiO_2 exhibiting a stronger Jahn-Teller distortion; XMCD (Figure 4) appears more sensitive to Jahn-Teller distortions than x-ray absorption (Figure 3), where the $S = \frac{1}{2}$ shapes are more similar for the two materials. The computed signature of $S = 1$ Ni species in LiNiO_2 (green in Figure 4) includes a sign change

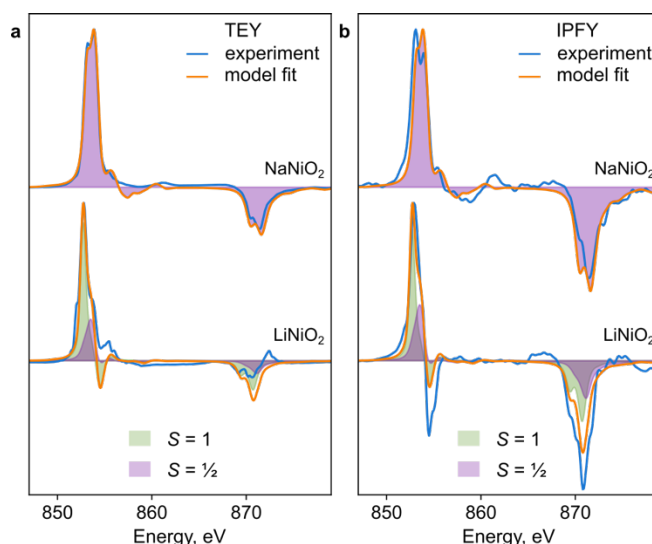


Figure 4: Ni L edge X-ray magnetic circular dichroism (XMCD) of LiNiO_2 and NaNiO_2 . (a) TEY, (b) IPFY. NaNiO_2 (top) was measured at 10 K and 8 T field, LiNiO_2 (bottom) was measured at 10 K and 8 T field. The models (orange) are fit using the same compositions as in Fig. 3. The XMCD signature of the spin-zero component is negligible. The calculated L_2 IPFY XMCD was scaled up by the same factor as the linear L_2 spectra in Fig. 3b. Raw spectra: Figure S1.

characteristic of spinel Ni^{2+} , as seen for NiFe_2O_4 spinel^{41,42}. This feature accounts for the lower-energy L_3 peak and sign change of the dichroism in LiNiO_2 relative to NaNiO_2 , especially in the more bulk-sensitive IPFY mode. The presence of about 10% excess reduced Ni species near the surface of LiNiO_2 observed in TEY mode relative to IPFY (Figure 3) prevents a more quantitative assignment of the LiNiO_2 TEY XMCD spectrum. Nevertheless, the differences between XMCD spectra of the two materials are consistent with the presence of $S = 1$ Ni in bulk LiNiO_2 due to disproportionation.

The $S = 0$ species does not possess an XMCD signature. We, therefore, verify its presence using the added dimension of inelastic energy loss in RIXS. The L_3 RIXS map of LiNiO_2 (Figure 5a) includes two features that distinguish it from prior reports of nickelate RIXS¹⁸. First, there is intensity approaching the elastic line near 853.5 eV, which is about 1 eV higher than in metallic NdNiO_3 ¹⁸. Second, features near 2 eV and 6 eV loss at 854 eV–

855 eV have not, to our knowledge, previously been reported. The fluorescence feature (dotted diagonal in Figure 5a) extends to < 1 eV loss at 852.0 eV, suggesting that LiNiO_2 possesses a nonzero optical bandgap¹⁸. To interpret the RIXS maps, we extended the same Anderson impurity model of three-fold disproportionation as used to interpret the XAS and XMCD data, without any additional optimization (Supplementary Information), and computed RIXS maps for three Ni species, weighted as for IPFY (Figure 3b). We discuss loss spectra at three incident photon energies, denoted (i)-(iii) in Figure 5a.

At 852.5 eV (Figure 5b, (i)), the main contributions come from $S = 1$ Ni species. This energy loss spectrum is similar to spectra of materials containing d^8 states, such as the binary oxide NiO ⁴³ and perovskite NdNiO_3 ¹⁸. Here, the model slightly over-estimates the crystal field splitting and reproduces the experimental spectrum with a slight shift to higher loss energies. However, surface reduction and the overlap of the main $d-d$ excitation with fluorescence near 1 eV loss may contribute to the mismatch here.

At 853.5 eV (Figure 5b (ii)), low-loss excitations attributed to $S = 1$ and $S = 1/2$ Ni species extend to the elastic line, consistent with the presence of states just below and above the Fermi level attributable to both species in DFT calculations (Extended Data Figure 2b). Broad states above 4 eV loss, above the fluorescence feature (seen at 2 eV loss for this photon energy) and attributable to $S = 1/2$ Ni species, likely arise from charge-transfer excitations, consistent with the d^8L contribution to its ground state.

Finally, at 854.5 eV (Figure 5b, (iii)) our model attributes the feature at 6 eV loss exclusively to $S = 0$ Ni species. The high energy loss of this component suggests it is also of charge-transfer origin, but this feature is not present in NdNiO_3 ¹⁸. Strong contributions of the $S = 0$ species are also evident at 2 eV loss. As at lower photon energies, the model slightly

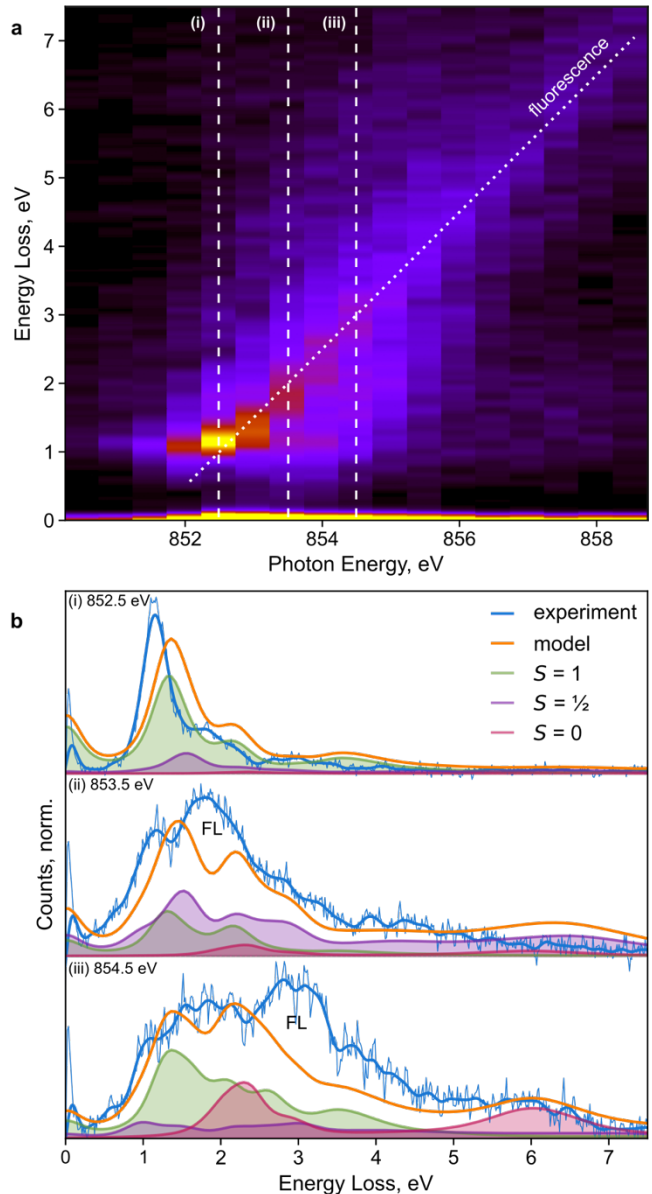


Figure 5: Ni L edge resonant inelastic x-ray scattering (RIXS) of LiNiO_2 . (a) RIXS intensity map measured across the L_3 edge at 20 K, (b) energy loss spectra (blue) at incident photon energies (i) 852.5 eV, (ii) 853.5 eV, and (iv) 855.0 eV compared to calculated loss spectra (orange). Calculated spectra were normalized to 85% of the maximum experimental intensity to account for the fluorescence feature (FL). Relative compositions of nickel species (green, purple, pink) were the same as for IPFY (Figure 3b). Full calculated $d-d$ and charge-transfer intensity maps are shown in Figure S5.

overestimates energy loss, but reproduces the major spectral features. We conclude that RIXS specifically detects the presence of $S = 0$ Ni species and confirms disproportionation in

LiNiO₂. Additional weak transitions at 1-2 eV loss above 856 eV (Figure 5a) are also attributable to the S = 0 Ni species (Supplementary Information). While additional fine-tuning of the charge-transfer multiplet model parameters is possible based on the RIXS spectra, we forego this here because of the contributions of reduced surface layers, which likely resemble NiO, to the main S = 1 feature, as in TEY (Figure 3a).

Consistency with observables

The model of dynamic and temperature-dependent disproportionation presented here is consistent with the five observed behaviors of LiNiO₂ detailed above, summarized in order:

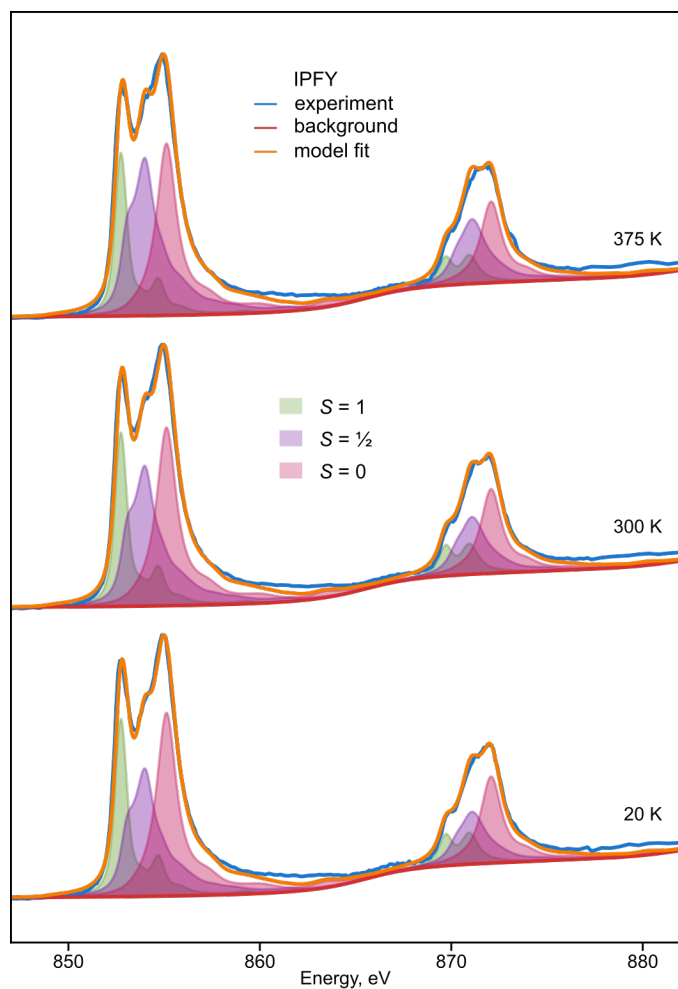
1. Additional S=1 Ni ions, arising from disproportionation with the NiO₂ layers, are predicted to stabilize Ni_{Li} defects through favorable antiferromagnetic (AFM) interactions (Supplementary Information), explaining the ubiquity of this antisite defect.
2. Activated electronic conduction plausibly arises from exchange (Figure 1a) between S = ½ and S = 1 Ni species. Indeed, the simulated free energy at the saddle point (Figure 2b) is close to half of the activation energy of electronic conductivity²³. The increase in this saddle-point energy as the S = ½ state predominates at high temperatures (Figure 2b) is consistent with increased activation of conductivity upon heating. Electron and hole polarons can be localized in the disproportionated structures, supporting a correspondence between formal spin and charge states (Supplementary Information). In contrast, in NaNiO₂, the collective Jahn-Teller distortion precludes the exchange of spin states and reduces electronic conductivity.
3. The small distortion of the LiNiO₂ unit cell is consistent with that of the limiting three-fold disproportionated cell, while the gradual decrease in this unit cell distortion with heating^{20,29} is consistent with the gradually increasing proportion of S = ½ species.
4. Previously not reported XMCD (Figure 4), Ni L₃ edge RIXS (Figure 5), and temperature-resolved XAS (Figure 2c) data provide strong experimental evidence for the disproportionation of Ni species in LiNiO₂. Accounting for S=0 and S=1 species affords an interpretation consistent across the Ni L-edge spectroscopies of LiNiO₂ (Figures 3-5) and of the spectroscopic differences between LiNiO₂ and NaNiO₂. These observations, combined with charge-transfer multiplet modelling, confirm a negative charge-transfer regime for both compounds⁴⁴, but highlight their distinct mechanisms of relieving degeneracy (Figure 1a).
5. The presence of S = 1 Ni species in bulk LiNiO₂ until 50% delithiation accounts for the increased Ni magnetic moments relative to those expected from formal Ni³⁺ in LiNiO₂³¹ and is further consistent with bulk-sensitive x-ray Raman scattering³⁶.

Conclusions

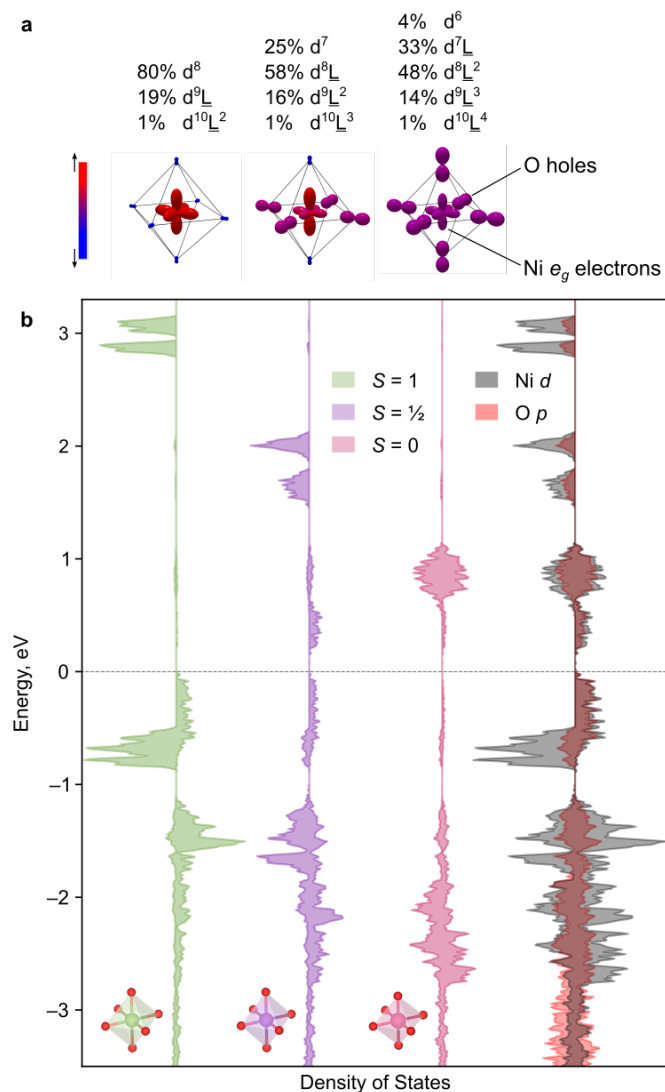
We have identified temperature-dependent dynamic disproportionation as the mechanism relieving orbital degeneracy in the archetypal layered nickelate LiNiO₂. Our results support a unified model where Ni species in LiNiO₂ exhibit three states with formal spins S = 0, S = ½, and S = 1 (which correspond to the formal oxidation states Ni⁴⁺, Ni³⁺, and Ni²⁺, respectively) and interconvert between these on a picosecond timescale. We have verified this behavior with characterization of the nickel L-edge using XAS, XMCD, and RIXS. The low-spin species exhibit strong Ni-O covalency within a charge-transfer multiplet model. These results enable the fingerprinting of the nickel L_{3,2} absorption edges based on first-principles calculations. The temperature dependence and dynamic nature of the disproportionation extend earlier models^{21,22} and allow for consistency with a diverse set of experimental observables:

thermally activated electronic conductivity²³, local structure from neutron diffraction²⁹, magnetometry³¹, stabilization of antisite Ni excess defects, and, more generally, the gradual changes in the properties of LiNiO₂ with heating and delithation. Overall, our unified picture of Ni behavior will advance

characterisation and understanding of the physics of nickelate materials for a range of applications, including rechargeable batteries, catalysis, and superconductivity.



Extended Data Figure 1: Temperature dependence of the IPFY spectra of LiNiO₂. The fitting of the IPFY spectra in Figure 2c with $S = \frac{1}{2}$ fractions 35%, 37%, and 41% at 20 K, 300 K, and 375 K, respectively, and the excess of $S = 1$ species over the $S = 0$ species is 3% at all temperatures. The difference between the fits to these spectra, collected at CLS, and those in Figure 3, collected at DLS, is 2% in both parameters at 300 K. The increasing smoothness of the LiNiO₂ spectra at the energies where the spectrum of the $S = \frac{1}{2}$ species has a maximum, in the middle of the edges, towards elevated temperature is further consistent with dynamic interconversion.



Extended Data Figure 2: Models of three Ni species in LiNiO_2 . (a) Bond length and charge-transfer multiplet components for each species, and Ni e_g electron and ligand hole density matrix plots. Salient features are high ionicity and low ligand hole content for the ($S = 1$), preferred occupancy of the $3z^2-r^2$ orbitals and bonding anisotropy consistent with Jahn-Teller distortions ($S = 1/2$), and spin depolarization and ligand hole contributions ($S = 0$). (b) Projected densities of Ni 3d states for $S = 1$ (green), $S = 1/2$ (purple), and $S = 0$ (pink) Ni species near the Fermi level. Right: total Ni 3d (grey) and O 2p (red) densities of states. The spin depolarization of the $S = 0$ states near 1 eV is consistent with the density matrix from ligand field calculations.

Methods

Sample preparation

Uncoated, polycrystalline LiNiO₂ powder was obtained from BASF. NaNiO₂ was prepared in house by a solid-state reaction. Appropriate molar amounts of Na₂CO₃ and NiO were ground together in a pestle and mortar, pressed into a pellet, and then heated at 650 °C under flowing O₂ for 12 hours. The heating and cooling rates were controlled at 10 °C min⁻¹. Powder X-ray diffraction data were collected for LiNiO₂ and NaNiO₂ on Cu-source Rigaku diffractometers. GSAS-II software was used to perform the Rietveld refinement analysis.

IPFY XAS and XMCD

Temperature dependent XAS measurements of LiNiO₂ were performed at the REIXS beamline of the Canadian Light Source (CLS). Samples were transported to the facility in sealed vials under argon atmosphere, pressed onto carbon tape on copper sample plates under argon atmosphere in a glovebox, and loaded into the x-ray experimental chamber without exposure to atmosphere. Measurements were performed at 20-375 K at pressures below 10⁻⁹ mBar. The incident beam was horizontally polarized and the normal of the sample plate was aligned with the beam. XAS was collected with TEY by monitoring sample drain current, and IPFY and PFY using a silicon drift detector with ~70 eV resolution. The silicon drift detector was positioned at an angle approximately 60 degrees from the sample normal.

Temperature dependent XMCD and XMLD measurements of LiNiO₂ and NaNiO₂ were performed in IPFY mode, with simultaneous TEY and FY detection at both the O K and Ni L_{3,2} edges on the high-field magnet end station at the I10 beamline, Diamond Light Source, UK. Powder and electrode samples were mounted onto a copper sample plate using carbon tape in an inert Ar-filled glovebox atmosphere, before being transported directly to the chamber in an Ar-filled sealed transfer vessel (avoiding exposure to air). Measurements were performed at 6-300K under ultra-high vacuum conditions. The incident beam was directed at a 60° angle to the normal of the sample plate. FY was acquired in the same 60° back-scattering geometry using a Si diode with an Al cover to filter out emitted electrons, mounted in front of the beam entrance port. IPFY was recorded with a four-element Vortex Si drift detector mounted at 90° to the incoming beam (30° to sample normal). XMCD and XMLD measurements were performed at 8 T and collected through the individual detection of right (σ_r) and left (σ_l) circular polarizations, or linear horizontal (σ_h) and vertical (σ_v) polarizations. The powdered form of the samples means we expect measured signals to be anisotropically averaged, i.e., significant orientation effects are not expected, although this likely reduces the observed extent of dichroism. Both O K-edges and Ni L_{3,2}-edges were measured in the continuous scanning mode of the monochromator, with an energy step size of 0.1 eV. All data was divided by the I₀ signal to remove top-up intensity spikes and energy-dependent intensity variations associated with the beamline. IPFY data was processed by summing the O emission signal over the incident energy range and following the procedure of Achkar et al.³⁵ The pre-edge average background was subtracted, and remaining intensity normalized by the post-edge average.

Ni L₃ edge RIXS

Ni L₃-edge RIXS spectra were measured at a temperature of 20 K at the I21 beamline, Diamond Light Source⁴⁵. The incident energy range was 849-859 eV in 0.5 eV steps. Samples were transferred to

the spectrometer using a vacuum-transfer suitcase to avoid air exposure and were pumped down to ultra-high vacuum (UHV) and left to fully degas overnight.

Computational: density-functional theory, ab initio molecular dynamics, cluster expansion

DFT simulations were carried out using the projector-augmented wave method⁴⁶⁻⁴⁸ in the VASP package^{49,50} using the meta-GGA functionals SCAN⁵¹ and r²SCAN⁵² and forgoing empirical parameters such as a Hubbard U correction or the fraction of exact exchange. The revised Vydrov-van Voorhis (rVV10) non-local dispersion correction was applied. As we were not aware of the accurate parameterization of the rVV10 correction for r²SCAN⁵³ until substantially after running extended ab initio molecular dynamics simulations using the parameterization for SCAN ($b=15.7$, $c=0.0063$)⁵⁴, and the favorability of disproportionation was sensitive to the functional over the dispersion correction, the molecular dynamics were not re-run. Static calculations were completed with the parameterization for r²SCAN ($b=11.95$, $c=0.0063$), 700 eV plane-wave cutoff, and 0.25 \AA^{-1} k -point spacing. Energies and forces were relaxed to 10^{-5} eV and 10^{-2} eV/ \AA , respectively, or better. Ab initio molecular dynamics (AIMD) simulations used a Γ -centered $2 \times 2 \times 2$ k -point mesh, 2 fs time steps, constant-volume (NVT) ensemble, Nosé-Hoover thermostat with a time constant of 40 steps, electronic convergence of 10^{-4} eV, and the preconditioned conjugate gradient algorithm (VASP ALGO=A), unless specified otherwise.

To identify the states of the Ni we use local spin densities, S , as calculated in VASP. This descriptor gives a relatively unambiguous assignment for each Ni without estimating formal charges from the full electronic density in post-processing. The first picosecond of every AIMD run was excluded from analyses for thermostat equilibration. The simulations at 100 K and 200 K, where sampling transitions between Ni states required long trajectories, were initialized by cooling from 300 K over 500 fs or longer. AIMD simulations with a Ni_{Li} defect were initialized with the starting spin of the antisite Ni set to $-2 \mu_B$, and all others as default ($1 \mu_B$). The trajectories of the nickel spins were binned into $S = 0$, $S = 1/2$, and $S = 1$ states by milestoning⁵⁵ with cutoffs of $0.2 \mu_B$, $0.7 \mu_B$, $1.02 \mu_B$, and $1.4 \mu_B$. A control simulation in the isobaric (NPT) ensemble was carried out with the Langevin thermostat coupled only to the Li atoms at 12 ps^{-1} to avoid perturbing the dynamics of Ni-O bonding.

A decorated cluster expansion of defect-free LiNiO₂ was trained to predict the nickel speciation on delithiation⁵⁶. Reference structures for training were chosen to be large enough to allow for disproportionation should that be favorable, and pre-distorted for accelerating relaxation. The DFT settings for reference structures were as for static calculations above, although some relaxations were shortened when clearly approaching convergence due to the reduced requirements on precision for the purposes of the cluster expansion. The root mean squared errors (RMSE) were 4.6 meV/f.u. over the training set and 5.6 meV/f.u. over the hold-out validation set. Charge-neutral grand canonical Monte-Carlo (CNGCMC) sampling was used to estimate the nickel speciation at all states of delithiation (Figure 2d), with spin states used as formal charge states for nickel. To mitigate the effects of commensurate lattice orderings⁵⁷ on predicted speciation, eight different supercell sizes were averaged. For each chemical potential of Li vacancies, the CNGCMC runs were initialized at 1000 K, cooled to 100 K for finding the ground state, heated to 500 K, and sampled for 10^6 steps, with the first half of those discarded. The concentrations of Ni species were averaged over supercells for each chemical potential of Li vacancies⁵⁸; chemical potentials of Ni species

were kept at zero relative to each other. A more detailed study of delithiation in LiNiO_2 and the limitations of the cluster expansion formalism is the subject of follow-on work.

Defect formation energies were calculated only for charge-neutral structures from relaxed defect-free and defect-incorporating cells^{59–62}. The chemical potentials of the elements at synthesis conditions were calculated from the energies of the reference phases^{62–64}. At the typical conditions of synthesis—1 atm O_2 pressure and 700 °C—the chemical potential of oxygen is $\mu_{\text{O}} = -1.065$ eV, which determines $\mu_{\text{Li}} = -2.962$ eV and $\mu_{\text{Ni}} = -1.379$ eV. We account for the antiferromagnetic–paramagnetic transition of NiO at its Néel temperature by taking the energy of paramagnetic NiO as the average of computed AFM and FM energies.

Multiplet ligand field theory modelling of the Ni $L_{3,2}$ edge spectroscopies

The nickel $L_{3,2}$ -edge multiplet ligand field theory (MLFT) simulations were performed using the many-body code Quancy.⁶⁵ The simulation was implemented using a single-cluster NiO_6 Hamiltonian of O_h symmetry for $S = 0, 1$ and D_{4h} symmetry for $S = 1/2$. The Ni 2p, Ni 3d, and ligand shells are explicitly included. For all calculations, Slater integrals are scaled to 80% and 85% for the initial and final Hamiltonians, respectively. Additionally, onsite ligand energy shifts of $T_{\text{pp}} = \pm 0.75$ eV were applied to the ligand orbitals of e_g (+) and t_{2g} (-) symmetry.

A charge transfer energy of $\Delta = -0.5$ eV assumed for the $3d^7$ $S = 1/2$ Ni, as used by Green et al.³⁷ This charge transfer energy, along with a Coulomb interaction energy of $U_{dd} = 6$ eV, leads to charge transfer energies of 5.5 eV and -6.5 eV for the $S = 1$ ($3d^8$) and $S = 0$ ($3d^6$) clusters, respectively. A core-valence Coulomb interaction parameter of $U_{pd} = 7$ eV was used, which is the standard ~ 1 eV larger than U_{dd} . Hopping integrals and crystal field energies are obtained directly from bond lengths using Harrison’s formulas^{37,66}, and hopping integrals were scaled by 80% in the XAS final state³⁷. The DFT-determined bond lengths were used for the three sites in LiNiO_2 . For NaNiO_2 , bond lengths of 1.93 Å and 2.16 Å for x/y and z bonds were used, respectively^{67–69}, which yields a slightly larger Jahn-Teller distortion than for the LiNiO_2 $S = 1/2$ site geometry. The charge transfer energies, hopping integrals, and crystal field potential energies are listed below for all calculations.

$S = 1$ calculation (eV): $\Delta = 5.5$, crystal field $10D_q = 0.71$, hopping integrals $V_{eg} = 2.63$, $V_{t2g} = 1.52$.

$S = 1/2$ calculation (eV): $\Delta = -0.5$, $10D_q = 0.78$ with Jahn-Teller splitting of $\Delta_{eg} = 0.15$ and $\Delta_{t2g} = 0.10$.

Here, Δ_{eg} denotes the difference between the $x^2 - y^2$ and $3z^2 - r^2$ onsite energies, and Δ_{t2g} the difference between the xy and xz/yz onsite energies (eV): $V_{3z^2-r^2} = 2.43$, $V_{x^2-y^2} = 3.33$, $V_{xz/yz} = 1.41$, $V_{xy} = 1.93$.

$S = 0$ calculation (eV): $\Delta = -6.5$, $10D_q = 0.93$, $V_{eg} = 3.456$, $V_{t2g} = 2.004$.

$S = 1/2$ calculation for NaNiO_2 (eV): $\Delta = -0.5$, $10D_q = 0.70$ with Jahn-Teller splitting of $\Delta_{eg} = 0.19$ and $\Delta_{t2g} = 0.12$. $V_{3z^2-r^2} = 2.02$, $V_{x^2-y^2} = 3.17$, $V_{xz/yz} = 1.17$, $V_{xy} = 1.84$.

Acknowledgements

The authors acknowledge funding from the UK Faraday Institution (faraday.ac.uk; EP/S003053/1, FIRG016, FIRG024) and the European Research Council (ERC) under the European Union’s Horizon 2020 research and innovation programme (EXISTAR, grant agreement No. 950598). B.J.M. acknowledges support from the Royal Society (URF/R/191006). R.S.W. acknowledges a CAMS-UK Fellowship through the Analytical Chemistry Trust Fund and a UKRI Future Leaders Fellowship

(MR/V024558/1). R.J.G. and G.H. acknowledge funding from the Natural Sciences and Engineering Research Council of Canada (NSERC). The authors acknowledge the HEC Materials Chemistry Consortium (EP/R029431) for the use of Archer2 high-performance computing (HPC) facilities. The authors also acknowledge the Faraday Institution's Michael HPC resource. We acknowledge Diamond Light Source for time on beamlines I10 and I21 under proposals MM33062 and MM30644-1, and Dr. Stefano Agrestini, Dr. Mirian Garcia-Fernandez, and Dr. Ke-Jin Zhou for assistance with the RIXS measurements. We acknowledge the support of the Royal Academy of Engineering under the Research Fellowship scheme. Part of the research described in this paper was performed at the Canadian Light Source, a national research facility of the University of Saskatchewan, which is supported by the Canada Foundation for Innovation (CFI), the Natural Sciences and Engineering Research Council (NSERC), the Canadian Institutes of Health Research (CIHR), the Government of Saskatchewan, and the University of Saskatchewan. A.D.P. is grateful to Dr. Pezhman Zarabadi-Poor and Dr. Gregory Rees for insightful discussions.

Author Contributions

Initial investigations of LiNiO_2 were carried by J.P.C. and extended to AIMD by A.D.P. with advice and supervision from M.S.I. and B.J.M. The temperature-dependent XAS experiments were proposed by A.D.P. and carried out by R.J.G. and R.S. (CLS). The XMCD experiments were proposed by R.J.G., J.E.N.S., R.S.W., and A.D.P., and carried out by A.D.P., J.E.N.S., L.A., and L.J. with P.B. (DLS). The RIXS experiments were proposed by A.D.P. and R.A.H. and carried out by R.A.H. with S.A., M.G.-F., K.-J.Z. Samples were prepared by R.A.H., L.A., J.E.N.S., and L.J. The charge-transfer multiplet modelling was carried out by G.H. and R.J.G. A.D.P. led the writing of the manuscript with input and contributions from all authors.

Supplementary Information

Characterization and experimental controls

TEY, TFY, IPFY comparison of LiNiO₂ and NaNiO₂

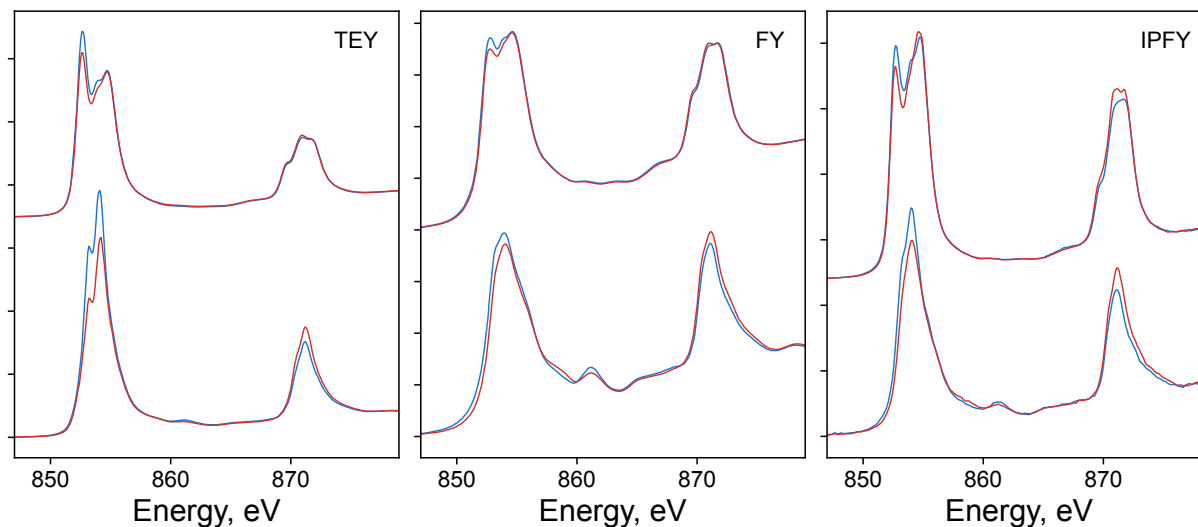


Figure S1: Ni soft x-ray absorption spectroscopy using three detection modes. (a) total electron yield, (b) fluorescence yield, (c) inverse partial fluorescence yield via emission at the O K-edge. Blue: σ_t polarisation, red: σ_r polarisation. Top: LiNiO₂, 6 K, 8 T. Bottom: NaNiO₂, 10 K, 8 T.

Absence of XMLD at the Ni edge and absence of dichroism at the O K edge

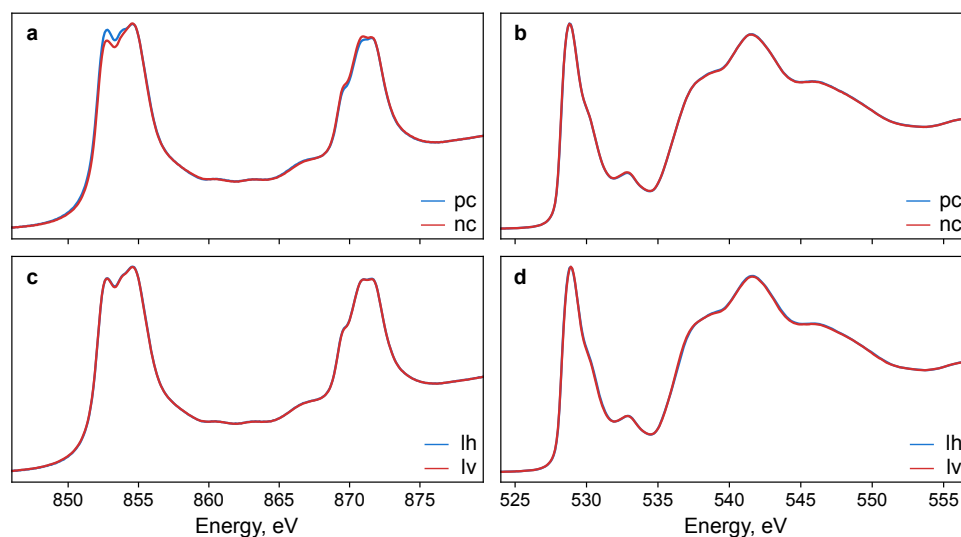


Figure S2: x-ray circular and linear dichroism in LiNiO₂. (a) circular, Ni L-edge, (b) circular, O K-edge, (c) linear, Ni L-edge, (d) linear, O K-edge. All: fluorescence yield, 6 K, 8 T. Only circular dichroism is observable, and only at the Ni L-edge.

XRD of LiNiO₂ and NaNiO₂ samples

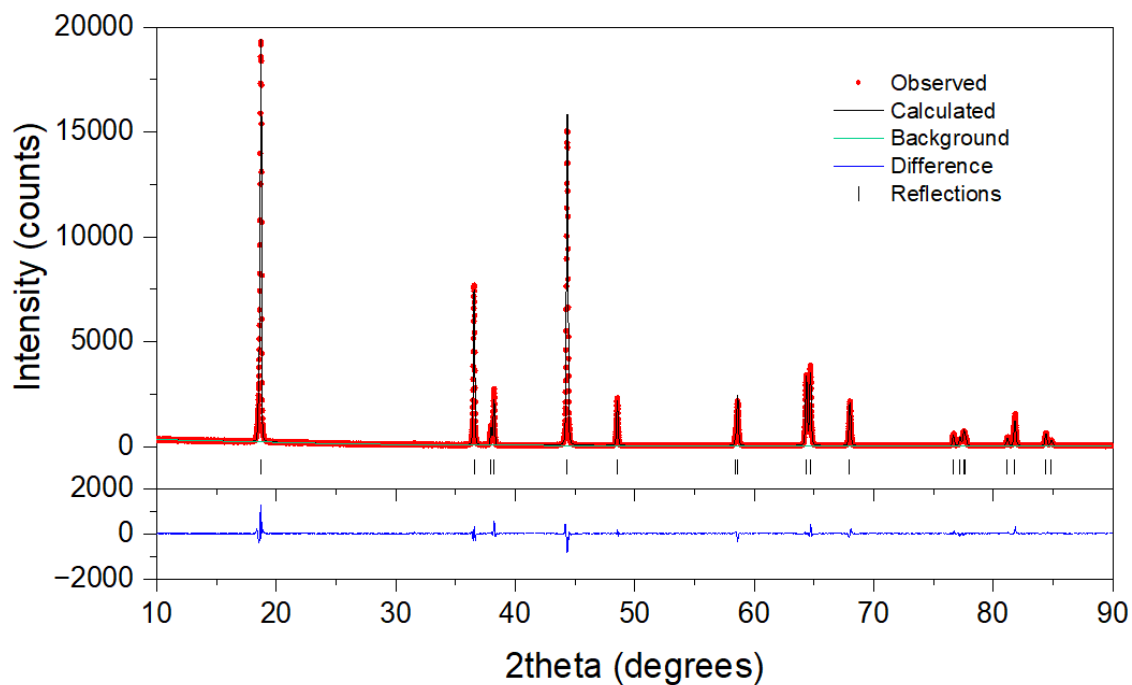


Figure S3. X-ray diffraction data for LiNiO₂.

Table S1. Rietveld refinement parameters for LiNiO₂.

	x	y	z	Occupancy	U _{iso}
Li	0.000	0.000	0.500	0.98(2)	0.006(2)
Ni	0.000	0.000	0.500	0.02(2)	0.013(2)
Ni	0.000	0.000	0.000	1.00	0.013(2)
O	0.000	0.000	0.260(1)	1.00	0.021(1)
Space Group: R-3m a = 2.879(1) c = 14.204(1)					
G.O.F. = 1.38 R _w = 9.13					

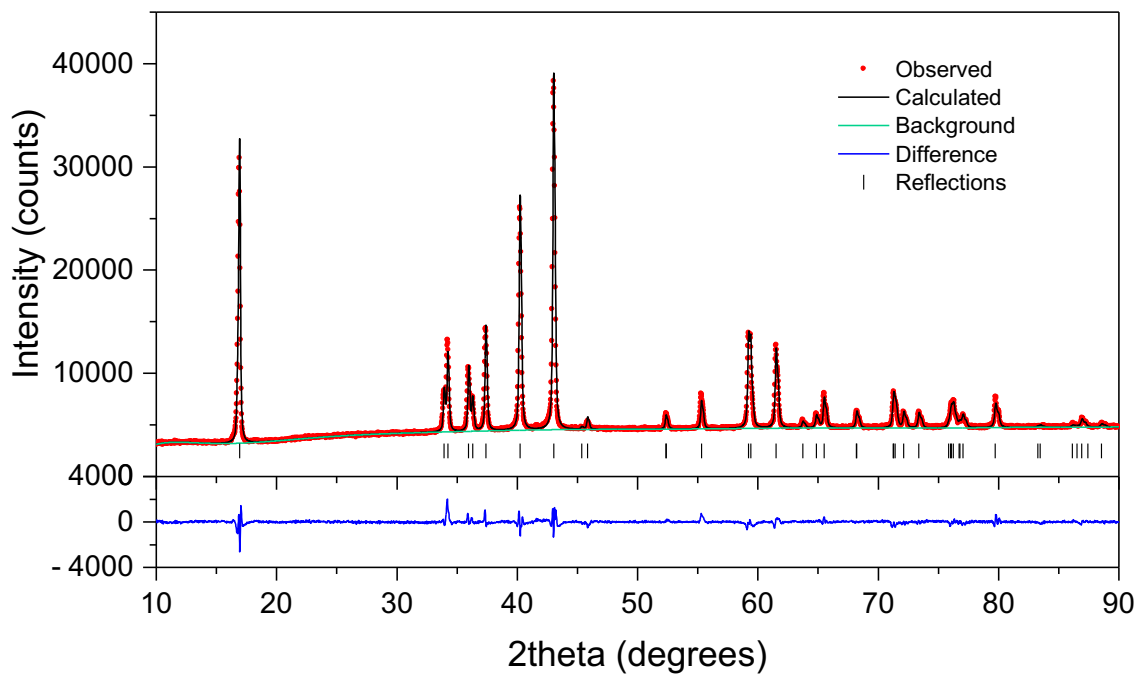


Figure S4. X-ray diffraction data for NaNiO_2 .

Table S2. Rietveld refinement parameters for NaNiO_2 .

	x	y	z	Occupancy	U_{iso}
Na	0.000	0.500	0.500	1.00	0.007(1)
Ni	0.000	0.000	0.000	1.00	0.031(1)
O	0.281(1)	0.000	0.791(1)	1.00	0.015(1)
Space Group: $C2/m$ $a = 5.327(1)$ $b = 2.847(1)$ $c = 5.587(1)$					
G.O.F. = 1.83 $R_w = 2.59$					

Calculated Resonant Inelastic X-ray Scattering Maps

RIXS maps calculated from the charge-transfer multiplet model above are shown in Figure S5. The scattered intensity near 857 eV photon energy and 2 eV loss is attributable to $S = 0$ Ni species.

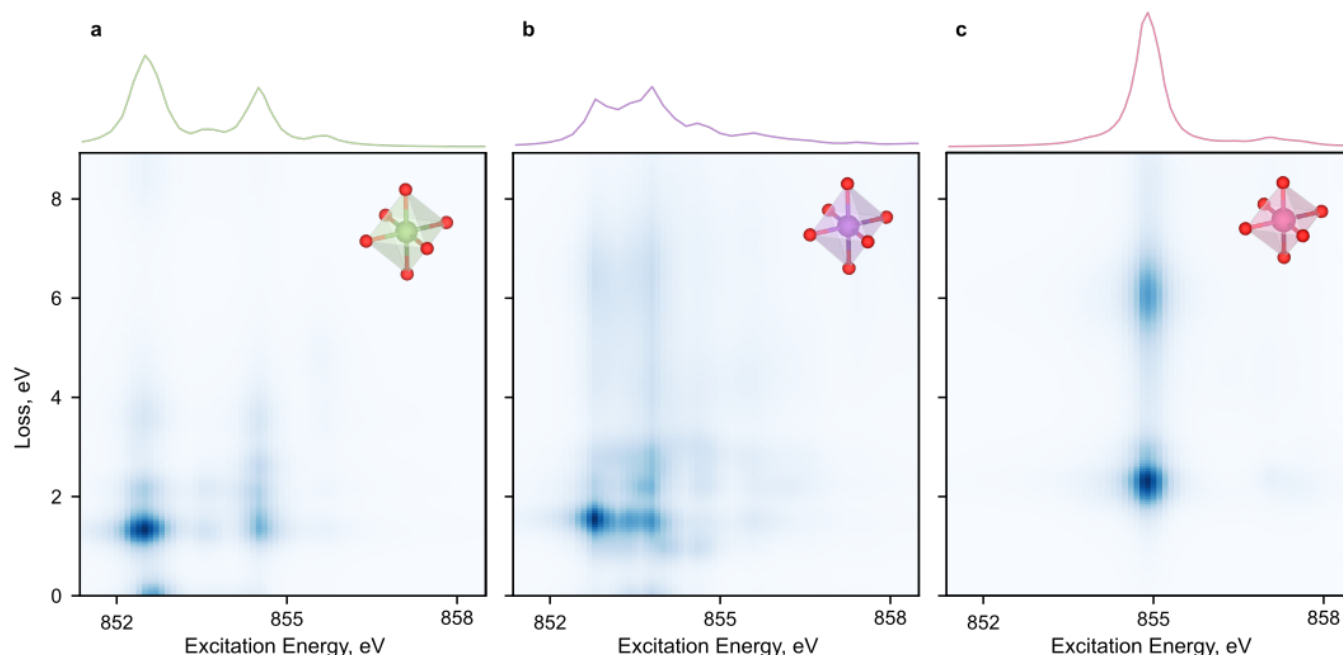


Figure S5: Calculated localized transitions in the Ni L_3 edge RIXS of LiNiO_2 . (a) $S = 1$ Ni species, (b) $S = \frac{1}{2}$ Ni species, (c) $S = 0$ Ni species. The integrated spectra are plotted above the intensity maps for each panel.

Choice of density functional using thermodynamic data

The geometries of NiO and LiNiO_2 simulated in small cells are close to experimental values^{11,70} and depend weakly on the choice of meta-GGA functionals (Table S3). The predicted thermodynamics and the geometry of NiO_2 depend more significantly on the choice of functional. Less expensive approaches such as PBE+U were discarded for their inability to accurately represent the c lattice contraction of the delithiated NiO_2 phase⁷¹. Even at the meta-GGA level of theory, a dispersion correction is necessary to reproduce the c lattice contraction of NiO_2 . Since fitted Hubbard U values are specific to oxidation states⁷², empirical + U corrections were avoided. In principle, the unusually large low-temperature heat capacity of LiNiO_2 makes a larger than normal contribution to room-temperature energies at 0.15 eV/f.u. for heating from 20 K to 300 K⁷³, but this correction was not applied here. SCAN over-stabilizes the NiO and LiNiO_2 phases, whereas $r^2\text{SCAN}$ offers a precise match to NiO thermodynamics, but both are used to perform ab initio molecular dynamics shown below. Overall, $r^2\text{SCAN}+r\text{VV10}$ best reproduced the thermodynamics of LiNiO_2 and its constituent phases^{74,75} and the geometry of the delithiated NiO_2 without major outlier errors.

Table S3: Comparison between structural and thermodynamic parameters of LiNiO₂ simulated with meta-GGA functionals and their experimental values.

Parameter	SCAN	SCAN +rVV10	r ² SCAN	r ² SCAN +rVV10	Exp't	Ref.
$R\bar{3}m$ a , Å	2.85	2.84	2.85	2.85	2.878	11
$R\bar{3}m$ c , Å	14.10	14.05	14.10	14.04	14.19	11
$R\bar{3}m$ ΔH , eV	-6.62	-6.74	-6.23	-6.40	-6.15	74
NiO a , Å	4.155	4.146	4.16	4.15	4.17	70
NiO ΔH , eV	-2.73	-2.80	-2.41	-2.51	-2.48	74
Li ₂ O ΔH , eV	-6.16	-6.21	-6.04	-6.09	-6.20	74
NiO ₂ a , Å	2.77	2.77	2.78	2.78	2.81	76
NiO ₂ c , Å	13.67	13.08	13.63	13.02	13.3	76

Disproportionation in geometry relaxations

The relaxed energy of the commonly computed zigzag P2₁/c phase is 83 meV/f.u. below the bulk-average $R\bar{3}m$ phase, consistent with previous studies¹⁹. However, in relaxations starting with the $R\bar{3}m$ phase we found a partial disproportionation of Ni spins from $S = 1/2$ to $S = 1$ and $S = 0$ for both SCAN and r²SCAN meta-GGA functionals. If all $S = 1/2$ Ni species are consumed and the resulting ($S = 1$, $S = 0$) pairs ordered linearly, such disproportionation yields the P2/c phase, previously predicted computationally^{19,21,77}. The similarity between the three interpenetrating transition-metal sublattices in the ground state of Li(NiMnCo)O₂³², the ground state of noncollinear spin models³³, and the disproportionated structure of AgNiO₂^{13,14}, which each exhibit three interpenetrating sublattices within the hexagonal layer of TMO₆ octahedra, suggests that the logical limit for disproportionation could be a phase where Ni species with spins $S = 1$, $S = 1/2$, and $S = 0$ similarly occupy three sublattices, a static version of which was proposed by Foyevtsova *et al.*²¹.

When this asymptotic three-fold disproportionated structure is relaxed, the volumes of the NiO₆ octahedra correlate with the spins of the Ni species: 10.9 Å³ for $S = 1$, 9.9 Å³ for $S = 1/2$, and 9.0 Å³ for $S = 0$ (Figure 2a), similar to AgNiO₂. All octahedra are somewhat distorted. The longest relaxed Ni–O bond is 2.06 Å, which is shorter than the Ni–O distance of 2.10 Å relaxed in the P2₁/c structure, and consistent with structural probes²⁹. The relaxed limiting three-fold disproportionated structure and the two-fold disproportionated P2/c structure have energies 14 meV/f.u. and 12 meV/f.u. above the zigzag P2₁/c structure, respectively. The energetic penalty for changing the ordering (clockwise vs anti-clockwise) of the three sublattices within adjacent NiO₂ layers is 5 meV/f.u., and antiferromagnetic (AFM) or ferrimagnetic (FiM) orderings carry penalties of about 1 meV/f.u.

Configurational entropy is expected to favor the three-fold disproportionated structure and other intermediate compositions over the fully comproportionated (P2₁/c or NaNiO₂-like monoclinic C2/m) and two-fold disproportionated P2/c endpoints. The cluster expansion model used in Figure 2d identifies the comproportionated all-spin-half LiNiO₂ as 11 meV/f.u. lower in energy than the three-fold disproportionated structure but does not predict it to be observable. The full exploitation of the cluster expansion model is the subject of follow-on work.

Dependence of Ni spin disproportionation on the choice of density functional

In the AIMD simulations of bulk pristine LiNiO_2 , or bulk LiNiO_2 with an antisite Ni_{Li} defect, substantial variation in spin was observed only for Ni. Spins on oxygens never exceeded $\approx 0.145 \mu_{\text{B}}$. However, the temperature dependence of the free energy as projected onto the Ni spin coordinate differed substantially with the choice of k-points and meta-GGA functionals.

First, we compare the free-energy surfaces from the reference simulation performed with a $2 \times 2 \times 2$ k-point mesh (Figure S6a, blue) versus a simulation performed at the Γ point exclusively (Figure S6a, pink) with the $r^2\text{SCAN}$ functional. The two free-energy surfaces are drastically different: the Γ -point simulation does not predict stable disproportionation or any thermally activated dynamics. In the Γ -point simulation, magnetic moments below $0.2 \mu_{\text{B}}$ or above $1.5 \mu_{\text{B}}$ are not realized. Figure S6a also shows that a small distortion of the cell angles acquired during the relaxation of the three-spin disproportionated structure perturbs the energy surface (Figure S6a, purple), making transitions slightly rarer relative to the symmetric hexagonal high-temperature cell (Figure S6a, blue). Performing the simulation in the isobaric ensemble has a similar effect (Figure S6a, green), and using a larger cell with 144 atoms instead of 108 as in all the other runs (Figure S6a, orange) predicts slightly smaller activation energies. Overall, the inclusion of off-zone-center k-points is critical to reproducing experimental observables.

Using the SCAN functional (Figure S6b) yields a nearly temperature-independent set of free-energy surfaces, in contrast with $r^2\text{SCAN}$. Using SCAN favors all-spin-half arrangements upon cooling,

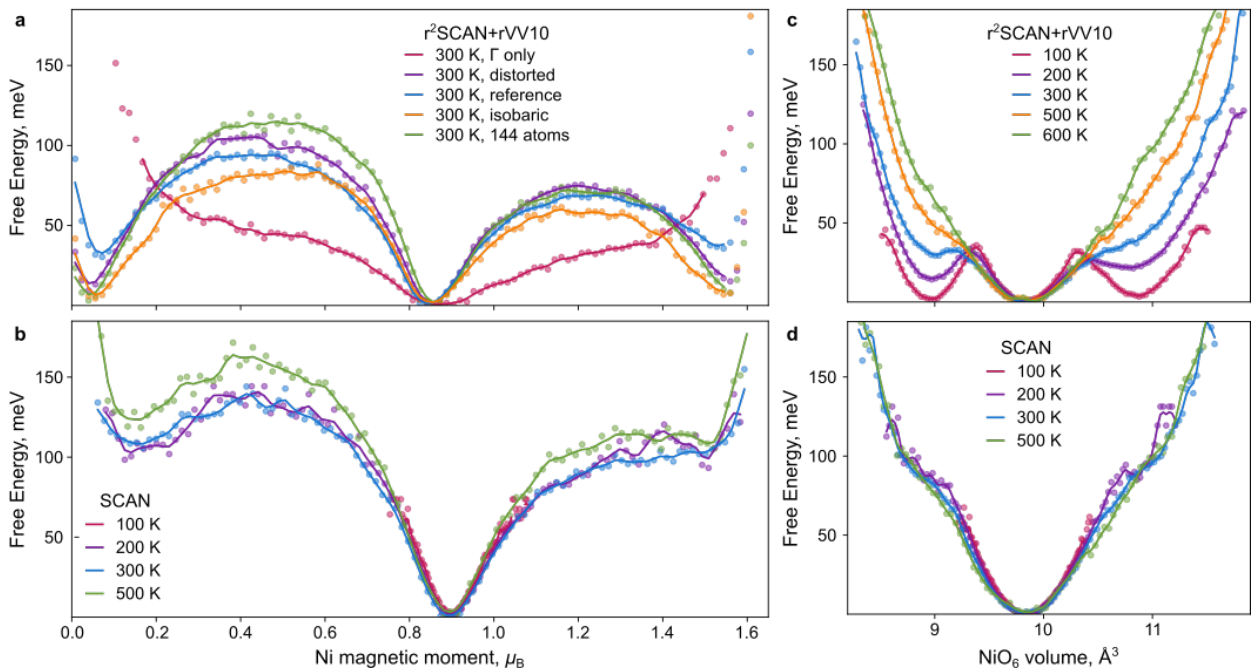


Figure S6: Sensitivity of simulated free energy surfaces to simulation parameters. (a) free energy surfaces versus the Ni magnetic moment with $r^2\text{SCAN+rVV10}$ at 300 K: reference as in Figure 3 (blue), relaxed cell with a small distortion (purple), hexagonal cell at the Γ point only (pink), hexagonal cell with 144 atoms (green), and simulation in the isobaric ensemble (orange). (b) free energy surfaces versus the Ni magnetic moment with SCAN and the hexagonal cell. (c-d) free energy surfaces versus the NiO_6 volume with $r^2\text{SCAN+rVV10}$ (c) or SCAN (d) and the hexagonal cell.

while r^2 SCAN favors disproportionation at cryogenic temperatures. The results from all functionals (r^2 SCAN and SCAN+rVV10 not shown) agree best at high temperatures and disagree most towards cryogenic temperatures. This can be further seen in the projections of free energy surfaces onto the NiO_6 octahedral volumes in Figure S6c for r^2 SCAN+rVV10 and Figure S6d for SCAN. This behavior of the simulated dynamics follows the trends in matching the thermodynamics of NiO and LiNiO_2 (Table S3): the choice of functional dominates the thermodynamic ensemble, simulation cell size, and non-local dispersion corrections.

We hypothesize that the sensitivity to the choice of functional is due to the small relative energy differences under investigation (<20 meV/f.u. between all relevant relaxed structures) being dominated by phonon energies (>60 meV) and the differences in predicted thermodynamic formation energies across functionals (e.g., 0.3–0.4 eV/f.u. for NiO, Table S3). This may represent a limit of precision for computational studies of LiNiO_2 structure and dynamics.

Structural Descriptors

The key observable structural signatures of local geometry are the unit cell parameters (Table S3) and the Ni-O bond length, which are typically probed by EXAFS^{7,27,28} and diffraction²⁹. These methods probe the average structure, and in both cases a fitting or refinement is required to obtain structural information. Several aspects complicate the use of structural information for fingerprinting Ni species: the primacy of the electronic coordinate, the noise in the structural coordinate, and the necessary regularization in interpreting experimental data. The electronic coordinate provides a stronger and lower-noise separation of the three Ni species (main text and Figure S6), and the NiO_6 octahedra of multiple species have the same bond lengths in static calculations. Despite drastically different predictions of Ni electronic speciation (Figure S6ab), the SCAN and r^2 SCAN functionals yield similar unit cell geometries (Table S3) and distributions of Ni-O bond lengths (Figure S7). The low-temperature bond length distributions are sharpest and provide the strongest contrast between functionals. The r^2 SCAN structures appear stiffer with narrower bond length distributions and have shorter long bonds. However, between 200 K and 300 K the two distinct bond populations merge so that by 300 K, the distributions of bond lengths are virtually

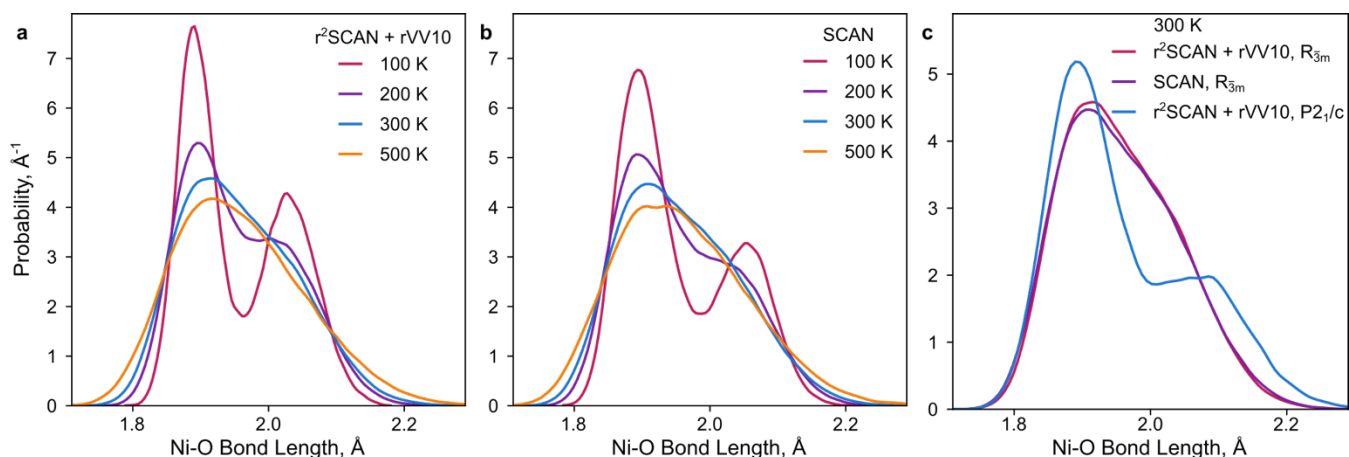


Figure S7: Simulated Ni-O bond distances in LiNiO_2 . (a) simulated with r^2 SCAN+rVV10 as a function of temperature, (b) simulated with SCAN as a function of temperature (c) at 300 K for two unit cells.

indistinguishable if the simulations are carried out in cell geometries relaxed from the hexagonal unit cell (Figure S7c), despite differences in the predicted electronic structure. Both hexagonal simulations yield long bonds at $\approx 2.05 \text{ \AA}$, in close agreement with experiment, for both electronic structures. By contrast, the zigzag structure ($P2_1/c$ in Figure S7c) predicts long bonds at $\approx 2.10 \text{ \AA}$, which is longer than any experimentally obtained ones.

Spin Transition Statistics

To verify whether the AIMD trajectories were of sufficient length to construct free energy surfaces, transitions between spin states were counted for each Ni ion by milestoning at 200 K and above (Methods). Simulations were continued until every ion had exhibited multiple transitions (Figure S8). Excluding the initial 1 ps for thermostat equilibration, the simulations at 200 K and 300 K were collected for over 10 ps with the longest residence times 7.7 ps at 200 K and 2.7 ps at 300 K. The trajectories at 500 K and 600 K were collected for at least 4.6 ps with the longest residence times 1.4 ps. At 300 K, the fastest transition times are on the order of 50 fs, close to one period of the Raman-active vibrations of Ni–O bonds⁷⁸. This is consistent with the coupling between NiO₆ geometry and Ni states: geometry changes mediated by vibrations set a speed limit on changes in electronic states.

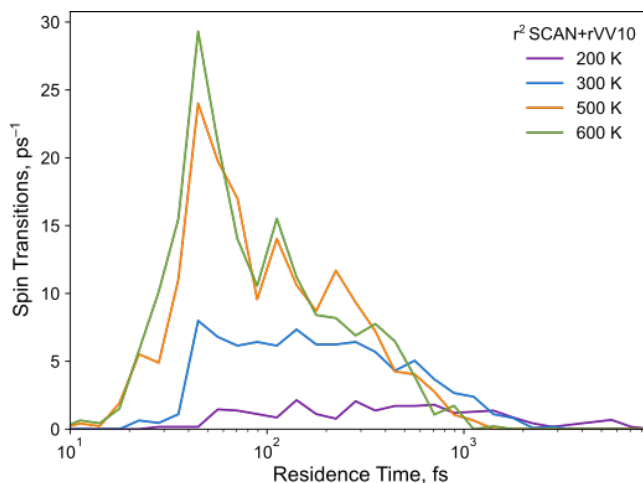


Figure S8: Spin transitions in ab initio molecular dynamics. The frequency of spin transitions is plotted versus the length of time the Ni ions spend in a particular spin state before making a transition.

Defect chemistry and stabilization of the Ni_{Li} antisite

We next explore the influence of disproportionation on defect chemistry via the localization of electronic charge carriers and the intrinsic antisite defect. Hole and electron polarons are relaxed in the limiting three-fold disproportionated structure by distorting the $S = \frac{1}{2}$ Ni octahedra to sizes commensurate with $S = 0$ and $S = 1$, respectively. While distortions of neighboring octahedra are minimal, some relaxations instead yield a reordering of the Ni spins and their respective octahedral volumes. Results are consistent between 108-atom and 144-atom supercells. The stabilization of polarons is consistent with a correspondence between the spin states and formal charge states of Ni species. By contrast, we have not been able to stabilize a hole polaron or a Ni with $S \approx 0$ in the $P2_1/c$ structure at the meta-GGA level of theory, except in a $2 \times 3 \times 2$ supercell (96 atoms) and surrounded by six opposite-sign $S = -\frac{1}{2}$ spins on adjacent Ni ions, which forms a partial superlattice like the three-fold disproportionation discussed here. This arrangement is clearly artificial, is energetically unfavorable relative to a delocalized hole, and is not stabilized in other supercells. Electron polarons are stable as $S = 1$ Ni in the $P2_1/c$ structure, consistent with earlier work⁶².

We now examine the Ni_{Li} antisite defect. To calculate the absolute defect formation energies, we first determine the chemical potentials of the elements from reference phase energies⁶⁴ (Figure S9ab). Accounting for the paramagnetic transition of NiO and representing the energetics

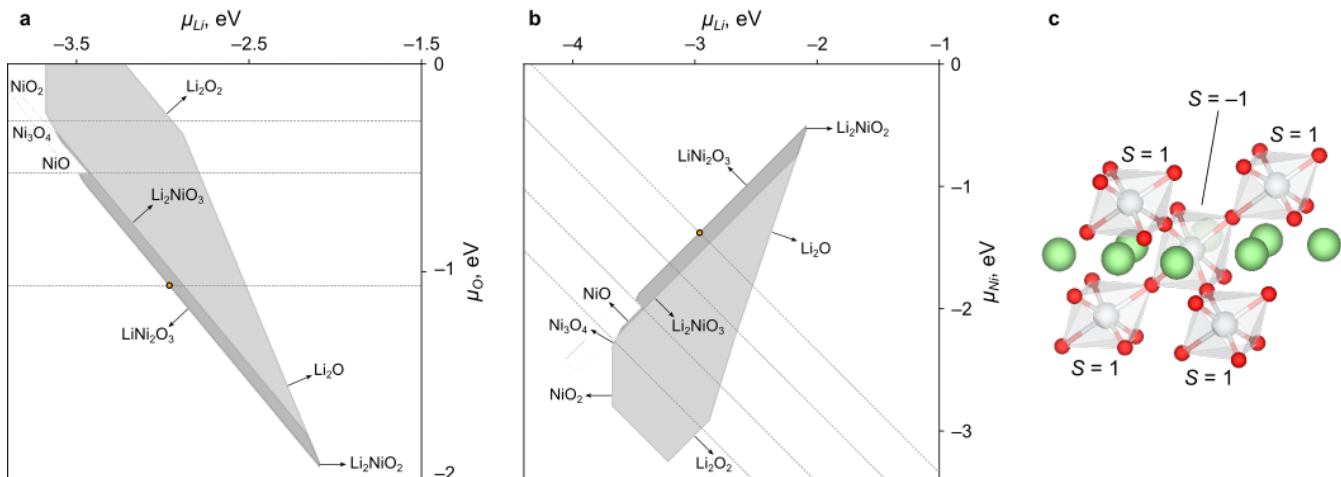


Figure S9: Phase and defect stability in $LiNiO_2$. (a,b) thermodynamic phase stability of disproportionated $LiNiO_2$, with competing phases highlighted, and the synthetic conditions denoted by an orange circle. (c) Antiferromagnetic stabilization of the Ni_{Li} antisite defect by $S = 1$ Ni ions.

of NiO accurately (Table S3) are key to estimating μ_{Li} and μ_{Ni} and the defect formation energy. The phase equilibrium at synthesis is between $LiNiO_2$ and a disordered rocksalt, computationally predicted as $LiNi_2O_3$ ⁷⁹. This is consistent with the experimental synthesis pathway from NiO via lithium insertion followed by the formation of ordered layers⁸⁰. Finally, since layered Li_2NiO_3 is not easily synthesized⁸¹, and not observed as a decomposition product, we include an additional region of likely metastability over Li_2NiO_3 (light grey in Figure S9ab).

Within disproportionated structures, the energy of the Ni_{Li} antisite depends on the arrangements of the nickel spins adjacent to it within the NiO_2 layers. The lowest-energy configuration for the Ni_{Li} defect is one where $S = -1$ Ni_{Li} is surrounded by $S = 1$ Ni ions via 180-degree Ni–O–Ni motifs (Figure S9c), reminiscent of antiferromagnetic NiO . At synthesis conditions, the formation energies of multiple configurations are negative, with the lowest at -60 meV, whereas the lowest defect energy in the $P2_1/c$ structure is 220 meV. In the $P2_1/c$ structure, only one Ni_{Ni} carries $S = 1$ to compensate the introduction of the Ni_{Li} . Our estimate of the formation energies for the most stable local configurations of Ni_{Li} is lower than the already low figures reported earlier⁶² due to accounting for this additional antiferromagnetic stabilization enabled by disproportionation in $LiNiO_2$.

While the local atomic and spin arrangements are expected to fluctuate rapidly at synthesis, the results remain relevant for room-temperature degradation pathways during battery operation. In AIMD trajectories incorporating a Ni_{Li} antisite, the Ni ions sharing octahedral corners with the defect as in Figure S9c carry $S = 1$ on average 50% more often than Ni ions away from the defect: the $S = 1$ that compensate the antisite are not free even at elevated temperatures. We conclude that magnetic stabilization contributes to the ubiquity of this pervasive defect. Ni_{Li} is stable not only because of the size match between Ni and Li, but also because of the ability of the Ni to disproportionate in the layered structure, which distinguishes it from Co and Mn oxides, and from the monoclinic $NaNiO_2$. This effect likely contributes to the driving forces for surface reconstructions and Ni migration into the Li layer during charging.

References (main text, methods, and SI)

1. Li, W., Erickson, E. M. & Manthiram, A. High-nickel layered oxide cathodes for lithium-based automotive batteries. *Nat Energy* **5**, 26–34 (2020).
2. Hales, N., Schmidt, T. J. & Fabbri, E. Reversible and irreversible transformations of Ni-based electrocatalysts during the oxygen evolution reaction. *Curr Opin Electrochem* **38**, 101231 (2023).
3. Chow, L. E. & Ariando, A. Infinite-Layer Nickelate Superconductors: A Current Experimental Perspective of the Crystal and Electronic Structures. *Front Phys* **10**, 1–8 (2022).
4. Sun, H. *et al.* Signatures of superconductivity near 80 K in a nickelate under high pressure. *Nature* **621**, 493–498 (2023).
5. Sood, A. *et al.* Electrochemical ion insertion from the atomic to the device scale. *Nat Rev Mater* **6**, 847–867 (2021).
6. Zhang, Z., Sun, Y. & Zhang, H. T. Quantum nickelate platform for future multidisciplinary research. *J Appl Phys* **131**, (2022).
7. Huang, H. *et al.* Unusual double ligand holes as catalytic active sites in LiNiO₂. *Nat Commun* **14**, 2112 (2023).
8. Bianchini, M., Roca-Ayats, M., Hartmann, P., Brezesinski, T. & Janek, J. There and Back Again—The Journey of LiNiO₂ as a Cathode Active Material. *Angewandte Chemie - International Edition* **58**, 10434–10458 (2019).
9. Mazin, I. I. *et al.* Charge ordering as alternative to Jahn-Teller distortion. *Phys Rev Lett* **98**, 1–4 (2007).
10. Uchigaito, H., Udagawa, M. & Motome, Y. Mean-field study of charge, spin, and orbital orderings in triangular-lattice compounds ANiO₂ (A = Na, Li, Ag). *J Physical Soc Japan* **80**, 1–10 (2011).
11. Dyer, L. D., Borie, B. S. & Smith, G. P. Alkali Metal-Nickel Oxides of the Type MNiO₂. *J Am Chem Soc* **76**, 1499–1503 (1954).
12. Chappel, E., Núñez-Regueiro, M. D., Chouteau, G., Isnard, O. & Darie, C. Study of the ferrodistorive orbital ordering in NaNiO₂ by neutron diffraction and submillimeter wave ESR. *Eur Phys J B* **17**, 615–622 (2000).
13. Wawrzyńska, E. *et al.* Charge disproportionation and collinear magnetic order in the frustrated triangular antiferromagnet AgNiO₂. *Phys Rev B* **77**, (2008).
14. Pascut, G. L. *et al.* Direct observation of charge order in triangular metallic AgNiO₂ by single-crystal resonant x-ray scattering. *Phys Rev Lett* **106**, 2–5 (2011).
15. Chung, J. H. *et al.* Possible charge disproportionation in 3R-AgNiO₂ studied by neutron powder diffraction. *Phys Rev B Condens Matter Mater Phys* **78**, 1–7 (2008).

16. Medarde, M. L. Structural, magnetic and electronic properties of RNiO₃ perovskites (R = rare earth). *Journal of Physics: Condensed Matter* **9**, 1679–1707 (1997).
17. Piamonteze, C. *et al.* Spin-orbit-induced mixed-spin ground state in RNiO₃ perovskites probed by x-ray absorption spectroscopy: Insight into the metal-to-insulator transition. *Phys Rev B* **71**, 2–5 (2005).
18. Bisogni, V. *et al.* Ground-state oxygen holes and the metal-insulator transition in the negative charge-transfer rare-earth nickelates. *Nat Commun* **7**, 1–8 (2016).
19. Sicolo, S., Mock, M., Bianchini, M. & Albe, K. And Yet It Moves: LiNiO₂, a Dynamic Jahn–Teller System. *Chemistry of Materials* **32**, 10096–10103 (2020).
20. Genreith-Schriever, A. R. *et al.* Jahn–Teller Distortions and Phase Transitions in LiNiO₂: Insights from Ab Initio Molecular Dynamics and Variable-Temperature X-ray Diffraction. *Chemistry of Materials* **36**, 2289–2303 (2024).
21. Foyevtsova, K., Elfimov, I., Rottler, J. & Sawatzky, G. A. LiNiO₂ as a high-entropy charge- and bond-disproportionated glass. *Phys Rev B* **100**, 165104 (2019).
22. Green, R. J. *et al.* Evidence for bond-disproportionation in LiNiO₂ from x-ray absorption spectroscopy. *arXiv:2011.06441* (2020).
23. Molenda, J., Wilk, P. & Marzec, J. Structural, electrical and electrochemical properties of LiNiO₂. *Solid State Ion* **146**, 73–79 (2002).
24. Molenda, J. & Stokłosa, A. Electronic and electrochemical properties of nickel bronze, Na_xNiO₂. *Solid State Ion* **38**, 1–4 (1990).
25. Shin, Y. J. *et al.* Influence of the Preparation Method and Doping on the Magnetic and Electrical Properties of AgNiO₂. *J Solid State Chem* **107**, 303–313 (1993).
26. Sörgel, T. & Jansen, M. Eine neue, hexagonale modifikation von AgNiO₂. *Z Anorg Allg Chem* **631**, 2970–2972 (2005).
27. Rougier, A., Delmas, C. & Chadwick, A. V. Non-cooperative Jahn-Teller effect in LiNiO₂: An EXAFS study. *Solid State Commun* **94**, 123–127 (1995).
28. Nakai, I., Takahashi, K., Shiraishi, Y., Nakagome, T. & Nishikawa, F. Study of the Jahn–Teller Distortion in LiNiO₂, a Cathode Material in a Rechargeable Lithium Battery, by in Situ X-Ray Absorption Fine Structure Analysis. *J Solid State Chem* **140**, 145–148 (1998).
29. Chung, J.-H. *et al.* Local structure of LiNiO₂ studied by neutron diffraction. *Phys Rev B* **71**, 064410 (2005).
30. Genreith-Schriever, A. R. *et al.* Jahn–Teller Distortions and Phase Transitions in LiNiO₂: Insights from Ab Initio Molecular Dynamics and Variable-Temperature X-ray Diffraction. *Chemistry of Materials* **36**, 2289–2303 (2024).

31. Mukai, K. *et al.* Structural and Magnetic Nature for Fully Delithiated Li_xNiO_2 : Comparative Study between Chemically and Electrochemically Prepared Samples. *The Journal of Physical Chemistry C* **114**, 8626–8632 (2010).
32. Kunnikuruvaan, S., Chakraborty, A. & Major, D. T. Monte Carlo- and Simulated-Annealing-Based Funneled Approach for the Prediction of Cation Ordering in Mixed Transition-Metal Oxide Materials. *The Journal of Physical Chemistry C* **124**, 27366–27377 (2020).
33. Miyashita, S. A Variational Study of the Ground State of Frustrated Quantum Spin Models. *J Physical Soc Japan* **53**, 44–47 (1984).
34. Varbaro, L. *et al.* Electronic Coupling of Metal-to-Insulator Transitions in Nickelate-Based Heterostructures. *Adv Electron Mater* **9**, 1–6 (2023).
35. Achkar, A. J. *et al.* Bulk sensitive x-ray absorption spectroscopy free of self-absorption effects. *Phys Rev B* **83**, 2–5 (2011).
36. An, L. *et al.* Distinguishing Bulk Redox from Near-Surface Degradation in Lithium Nickel Oxide Cathodes. 1–36 (2024) doi:10.26434/chemrxiv-2024-79nbz.
37. Green, R. J., Haverkort, M. W. & Sawatzky, G. A. Bond disproportionation and dynamical charge fluctuations in the perovskite rare-earth nickelates. *Phys Rev B* **94**, 1–5 (2016).
38. DiMucci, I. M. *et al.* Scrutinizing formally Ni IV centers through the lenses of core spectroscopy, molecular orbital theory, and valence bond theory. *Chem Sci* 1–37 (2023) doi:10.1039/D3SC02001K.
39. van der Laan, G. & Figuerao, A. I. X-ray magnetic circular dichroism - A versatile tool to study magnetism. *Coord Chem Rev* **277**, 95–129 (2014).
40. Green, R. J., Haverkort, M. W. & Sawatzky, G. A. Bond disproportionation and dynamical charge fluctuations in the perovskite rare-earth nickelates. *Phys Rev B* **94**, 1–5 (2016).
41. van der Laan, G. *et al.* Orbital polarization in NiFe_2O_4 measured by Ni-2p x-ray magnetic circular dichroism. *Phys Rev B* **59**, 4314–4321 (1999).
42. Saha, S. *et al.* Near-surface electronic structure in strained Ni-ferrite films: An x-ray absorption spectroscopy study. *Journal of Vacuum Science & Technology A* **42**, (2024).
43. Ghiringhelli, G. *et al.* Observation of two nondispersive magnetic excitations in NiO by resonant inelastic soft-X-ray scattering. *Phys Rev Lett* **102**, 2–5 (2009).
44. Kuiper, P., Kruizinga, G., Ghijsen, J., Sawatzky, G. A. & Verweij, H. Character of Holes in $\text{Li}_x\text{Ni}_{1-x}\text{O}$ and Their Magnetic Behavior . *Phys Rev Lett* **62**, 1214–1214 (1989).
45. Zhou, K.-J. *et al.* I21: an advanced high-resolution resonant inelastic X-ray scattering beamline at Diamond Light Source. *J Synchrotron Radiat* **29**, 563–580 (2022).
46. Blöchl, P. E. Projector augmented-wave method. *Phys Rev B* **50**, 17953–17979 (1994).

47. Kresse, G. & Furthmüller, J. Efficiency of ab-initio total energy calculations for metals and semiconductors using a plane-wave basis set. *Comput Mater Sci* **6**, 15–50 (1996).
48. Kresse, G. & Furthmüller, J. Efficient iterative schemes for ab initio total-energy calculations using a plane-wave basis set. *Phys Rev B* **54**, 11169–11186 (1996).
49. Kresse, G. & Hafner, J. Ab initio molecular dynamics for liquid metals. *Phys Rev B* **47**, 558–561 (1993).
50. Kresse, G. & Hafner, J. Ab initio molecular-dynamics simulation of the liquid-metal–amorphous-semiconductor transition in germanium. *Phys Rev B* **49**, 14251–14269 (1994).
51. Sun, J., Ruzsinszky, A. & Perdew, J. P. Strongly Constrained and Appropriately Normed Semilocal Density Functional. *Phys Rev Lett* **115**, 036402 (2015).
52. Furness, J. W., Kaplan, A. D., Ning, J., Perdew, J. P. & Sun, J. Accurate and Numerically Efficient r2SCAN Meta-Generalized Gradient Approximation. *Journal of Physical Chemistry Letters* **11**, 8208–8215 (2020).
53. Ning, J. *et al.* Workhorse minimally empirical dispersion-corrected density functional with tests for weakly bound systems: R2SCAN+rVV10. *Phys Rev B* **106**, 1–14 (2022).
54. Peng, H., Yang, Z. H., Perdew, J. P. & Sun, J. Versatile van der Waals density functional based on a meta-generalized gradient approximation. *Phys Rev X* **6**, 1–15 (2016).
55. Hartich, D. & Godec, A. Violation of Local Detailed Balance Despite a Clear Time-Scale Separation. *arXiv:2111.14734* (2021).
56. Barroso-Luque, L. *et al.* smol: A Python package for cluster expansions and beyond. *J Open Source Softw* **7**, 4504 (2022).
57. Mock, M., Bianchini, M., Fauth, F., Albe, K. & Sicolo, S. Atomistic understanding of the LiNiO₂–NiO₂ phase diagram from experimentally guided lattice models. *J Mater Chem A Mater* **9**, 14928–14940 (2021).
58. Zhong, P., Xie, F., Barroso-Luque, L., Huang, L. & Ceder, G. Modeling Intercalation Chemistry with Multiredox Reactions by Sparse Lattice Models in Disordered Rocksalt Cathodes. *PRX Energy* **2**, 043005 (2023).
59. Zhang, S. & Northrup, J. Chemical potential dependence of defect formation energies in GaAs: Application to Ga self-diffusion. *Phys Rev Lett* **67**, 2339–2342 (1991).
60. Lany, S. & Zunger, A. Accurate prediction of defect properties in density functional supercell calculations. *Model Simul Mat Sci Eng* **17**, (2009).
61. Freysoldt, C., Neugebauer, J. & Van De Walle, C. G. Fully Ab initio finite-size corrections for charged-defect supercell calculations. *Phys Rev Lett* **102**, 1–4 (2009).

62. Hoang, K. & Johannes, M. D. Defect chemistry in layered transition-metal oxides from screened hybrid density functional calculations. *J Mater Chem A Mater* **2**, 5224–5235 (2014).
63. Reuter, K. & Scheffler, M. Composition, structure, and stability of RuO₂(110) as a function of oxygen pressure. *Phys Rev B* **65**, 035406 (2001).
64. Buckeridge, J., Scanlon, D. O., Walsh, A. & Catlow, C. R. A. Automated procedure to determine the thermodynamic stability of a material and the range of chemical potentials necessary for its formation relative to competing phases and compounds. *Comput Phys Commun* **185**, 330–338 (2014).
65. Haverkort, M. W. Quanta for core level spectroscopy - excitons, resonances and band excitations in time and frequency domain. *J Phys Conf Ser* **712**, 012001 (2016).
66. Wills, J. M. & Harrison, W. A. Interionic interactions in transition metals. *Phys Rev B* **28**, 4363–4373 (1983).
67. Dyer, L. D., Borie, B. S. & Smith, G. P. Alkali Metal-Nickel Oxides of the Type MNiO₂. *J Am Chem Soc* **76**, 1499–1503 (1954).
68. Chappel, E., Núñez-Regueiro, M. D., Chouteau, G., Isnard, O. & Darie, C. Study of the ferrodistorive orbital ordering in NaNiO₂ by neutron diffraction and submillimeter wave ESR. *Eur Phys J B* **17**, 615–622 (2000).
69. Vassilaras, P., Ma, X., Li, X. & Ceder, G. Electrochemical Properties of Monoclinic NaNiO₂. *J Electrochem Soc* **160**, A207–A211 (2013).
70. Cheetham, A. K. & Hope, D. A. O. Magnetic ordering and exchange effects in the antiferromagnetic solid solutions M_xNi_{1-x}O. *Phys Rev B* **27**, 6964–6967 (1983).
71. Chakraborty, A., Dixit, M., Aurbach, D. & Major, D. T. Predicting accurate cathode properties of layered oxide materials using the SCAN meta-GGA density functional. *NPJ Comput Mater* **4**, 46–49 (2018).
72. Kowalski, P. M. *et al.* Fundamentals of energy storage from first principles simulations: Challenges and opportunities. *Front Energy Res* **10**, 1–14 (2023).
73. Kawaji, H. *et al.* Low-temperature heat capacity of layer structure lithium nickel oxide. *Solid State Ion* **152–153**, 195–198 (2002).
74. Wang, M. & Navrotsky, A. Enthalpy of formation of LiNiO₂, LiCoO₂ and their solid solution, LiNi_{1-x}CoxO₂. *Solid State Ion* **166**, 167–173 (2004).
75. Kawaji, H. *et al.* Low-temperature heat capacity of layer structure lithium nickel oxide. *Solid State Ion* **152–153**, 195–198 (2002).
76. Mock, M., Bianchini, M., Fauth, F., Albe, K. & Sicolo, S. Atomistic understanding of the LiNiO₂–NiO₂ phase diagram from experimentally guided lattice models. *J Mater Chem A Mater* **9**, 14928–14940 (2021).

77. Chen, H., Freeman, C. L. & Harding, J. H. Charge disproportionation and Jahn-Teller distortion in LiNiO₂ and NaNiO₂: A density functional theory study. *Phys Rev B* **84**, 1–7 (2011).
78. Flores Cedeño, E. J. Development of operando diagnostics for Li-ion cathodes by Raman spectroscopy. (ETH Zürich, 2019). doi:10.3929/ethz-b-000373382.
79. Das, H., Urban, A., Huang, W. & Ceder, G. First-Principles Simulation of the (Li-Ni-Vacancy)O Phase Diagram and Its Relevance for the Surface Phases in Ni-Rich Li-Ion Cathode Materials. *Chemistry of Materials* **29**, 7840–7851 (2017).
80. de Biasi, L. *et al.* Phase Transformation Behavior and Stability of LiNiO₂ Cathode Material for Li-Ion Batteries Obtained from In Situ Gas Analysis and Operando X-Ray Diffraction. *ChemSusChem* **12**, 2240–2250 (2019).
81. Bianchini, M. *et al.* From LiNiO₂ to Li₂NiO₃: Synthesis, Structures and Electrochemical Mechanisms in Li-Rich Nickel Oxides. *Chemistry of Materials* **32**, 9211–9227 (2020).